THE IMPACT OF CANOPY GEOMETRY ON PARTICLE DISPERSION GRADIENTS IN SPARSE AGRICULTURAL CANOPIES

by

Brian Bailey

A thesis submitted to the faculty of
The University of Utah
in partial fulfillment of the requirements for the degree of

Master of Science

Department of Mechanical Engineering

The University of Utah

May 2011

The University of Utah Graduate School

STATEMENT OF THESIS APPROVAL

The thesis of **Brian Bailey**

has been approved by the following supervisory committee members:

James R. Stoll II , Chair **14 March 2011**
Date Approved

Eric R. Pardyjak , Member **14 March 2011**
Date Approved

Meredith M. Metzger , Member **14 March 2011**
Date Approved

and by **Tim Ameel** , Chair of

the Department of **Mechanical Engineering**

and by Charles A. Wight, Dean of The Graduate School.

ABSTRACT

Turbulent dispersion is one of the most important transport mechanisms in the life cycle of many fungal plant pathogens. Without turbulent dispersion, inoculum spread would be confined to adjacent leaves, limiting the severity of epidemics. Thus, understanding the mechanisms that influence and control dispersion from disease foci are of primary importance towards improving our ability to prevent and respond to disease outbreaks. In sparse canopy environments, the influence of canopy geometry (row spacing, canopy height, and plant density) on turbulent fluxes can be problematic for traditional dispersion modeling techniques that rely on assumptions of steady or horizontally homogeneous velocity fields. Here, the link between canopy geometry, turbulent fluxes and particle dispersion gradients in sparse agricultural canopies was explored using a Lagrangian particle dispersion model linked to velocity fields from large-eddy simulations. In particular, particle dispersion from line sources in plant canopies with geometry characteristic of grape vineyards were examined. Simulations were performed with varying row spacing and plant density to characterize particle dispersion within the canopy over a large range of length scales. It was of primary importance to examine how changing plant geometry could limit the spread of pathogens over large length scales, thus limiting the speed at which epidemics spread. Unresolved particle motion was modeled by solving a form of the Langevin equation and particle deposition onto vegetation is modeled using a stochastic technique.

Results show that as overall canopy density decreases, bulk velocity in the canopy increases exponentially. This has a substantial impact on particle concentrations downstream of the source, as mean particle velocity influences concentrations. Furthermore, as canopy density decreases, particles tend to travel further before being deposited. However, as canopy density decreases, fewer particles tend to escape the canopy, which corresponds to a lower probability of long-distance transport. Thus, in less dense geometries, particles tend to spread further in near-source areas inside

the canopy, but transport is more likely to be confined to smaller length scales. More dense canopies tend to limit transport near the source due to increased drag and deposition, but increased canopy escape increases the probability of transport over large length scales.

For my wonderful parents.

CONTENTS

LIST OF FIGURES

LIST OF TABLES

CHAPTER 1

INTRODUCTION

The increase in manufacturing and technology has widely shaped the modern world we live in. However, one cannot neglect the central role plants play in the life of every human and animal. Plants make up all of the food in which all animals consume, directly or indirectly. Not only do humans eat plants, the animals humans eat also feed on plants. Consequentially, sustaining the productivity of the agricultural industry is of great importance. A secure food supply is important, not only for feeding the human population, but also because of its importance in the local and global economy.

The spread of disease-causing pathogens in plant canopies is an important factor in the volume and quality of crop yield. Plants become infected by pathogenic microorganisms in a very similar way that humans become infected. Disease outbreaks can be detrimental economically to growers and impact the security of the food supply. It is estimated that diseases interfere with or destroy approximately 15% of crops produced globally, which accounts for losses totaling about $220 billion [1]. The ability for growers to limit the spread of disease within agricultural canopies can be directly linked to the quality and quantity of crop yield.

1.1 Plant Pathology

This research focuses on the spread of disease in agricultural canopies, specifically the transport of *Erysiphe necetor* (powdery mildew of *Vitis vinifera L.*, grapes) spores in grape vineyards. The severity of diseases caused by pathogens are strongly linked to the distance and speed that spores can travel from initial sources of inoculum. Without dispersion, many epidemics would not progress [34]. Spores have no way of physically transporting themselves and must be carried by moving objects or materials. One mechanism for spore spread is transport by attachment to physical objects which move [1] (i.e., water, living organisms, farming equipment, etc.) In

general, this mechanism offers relatively slow transport which occurs over small scales [34]. Another mechanism which offers greater potential for epidemic spread is wind transport [1]. The turbulent ABL can transport large quantities of spores across large length scales, making it the primary transport mechanism for many pathogens [5, 34]. Therefore, understanding turbulent transport of spores is of primary importance toward understanding plant disease epidemiology.

For perennial plants like grape vines, the existence of the plant canopy has a strong impact on turbulent fluxes [16] and presumably on spore transport through the canopy. While a strong understanding of how continuous canopies impact turbulent transport processes and flow structures has started to develop [16, 17, 47, 49, 53], the same cannot be said of discontinuous or sparse canopies where a substantial percentage of the canopy is open. Motivated by the importance of turbulent transport in epidemic development and by the sparse nature of most vineyards, this research examines how plant canopy geometry (specifically row spacing and plant density) interacts with atmospheric flow characteristics to impact the dispersion of airborne plant pathogen spores in grape vineyards using a computational model.

1.2   Methods for the Simulation of Canopy Flows

Numerical simulations can be a valuable tool for understanding and analyzing the flow field in and above canopies. Field experiments can be expensive and time-consuming and can result in sparse data sets. They also limit studies to physical geometries and conditions that are currently available to the experimentalist. Numerical simulations can be conducted for a wide variety of flow conditions and geometries in a relatively short period of time. They also generally provide much more finely resolved data than experiments, with the limiting factor being the accuracy of turbulence models and the ability to specify boundary and initial conditions.

The simulation of the turbulent atmospheric boundary layer can pose many challenges due to the complexity of the flow. Furthermore, the addition of a sparse vegetative canopy to the simulation domain can present additional complications. Some of these challenges, as well as their implications on available simulation methods will be presented in the following sections.

1.2.1   Simulation of Turbulent Flows

The complexity of turbulent flows makes numerical simulation a challenging task. The velocity field is three-dimensional, time-dependent, and random-like. Furthermore, there exists a wide range of length scales in turbulent flow, the largest on the order of the characteristic width of the flow and the smallest being the Kolmogorov length. The ratio of the smallest to largest scales in the flow scales as $Re^{-3/4}$ [44]. Thus, as the Reynolds number increases, the smallest scales becomes smaller and the range of length scales becomes larger. In turbulent flow simulations, all length scales must be resolved or modeled. Atmospheric flows have a large Reynolds number ($> 10^5$), and have a corresponding Kolmogorov length scale on the order of 1 mm. Any length scales that are not explicitly resolved in the simulation must instead be modeled [44]. Such models can be difficult to formulate considering they must accurately represent the complex dynamics of turbulent flows as generally as possible. Since most models are not able to generalize to any arbitrary flow, models are commonly applicable to only limited types of flows to which they have been tailored.

1.2.2   Governing Equations

General atmospheric flow is governed by the Navier-Stokes equations, in which a set of equations are solved for the air velocity components and possibly scalars of interest. The first important equation in the set is the conservation of mass equation, which can be written as

$$\frac{D\rho}{Dt} + \rho\frac{\partial u_i}{\partial x_i} = 0, \tag{1.1}$$

where t is time, u_i (i = 1, 2, 3 = stream-wise, span-wise, vertical) represents the three components of the velocity, x is the spatial coordinate system, and ρ is air density, and D/Dt is the material derivative. For canopy flows, the air can be approximated as incompressible, thus $D\rho/Dt = 0$. With this assumption, eqn. 1.1 becomes

$$\frac{\partial u_i}{\partial x_i} = 0. \tag{1.2}$$

Momentum transport is governed by the following linked set of equations (written in nondimensional form):

$$\frac{\partial u_i}{\partial t} + \frac{\partial u_i u_j}{\partial x_j} = -\delta_{i3}\frac{T_v - \langle T_v \rangle}{T_o}\hat{g} + \frac{1}{Ro}\epsilon_{ij3}u_j - \frac{\partial p}{\partial x_i} + \frac{1}{Re}\frac{\partial^2 u_j}{\partial x_j^2} + F_i, \qquad (1.3)$$

where t is time, u_i (i=1,2,3) represents the three components of the velocity, x is the spatial coordinate system, T_v is potential temperature where the angle brackets represent a horizontal average, T_o is a buoyancy reference temperature, g is the acceleration due to gravity, δ is the Kronecker delta tensor, Ro is the Rossby number, ϵ is the permutation tensor, p is the nondimensional pressure, Re is the Reynolds number, and F_i is a general forcing term. Buoyancy effects are modeled using the Boussinesq approximation [37], and rotational effects have been considered.

When eqn. 1.3 is applied specifically to canopy flows, several simplifications can be made.

1. If only neutral flow is considered, buoyancy effects become negligible and the buoyancy term can be eliminated.

2. For domain heights of a few canopy heights, the Rossby number is generally large and rotational effects can be neglected.

3. Since the Reynolds number is very large for canopy flows, molecular diffusion can be neglected.

With these assumptions, eqn. 1.3 reduces to

$$\frac{\partial u_i}{\partial t} + \frac{\partial u_i u_j}{\partial x_j} = -\frac{\partial p}{\partial x_i} + F_i. \qquad (1.4)$$

Using the previous assumptions, an equation for the transport of a general scalar can be written as

$$\frac{\partial \theta}{\partial t} + \frac{\partial u_j \theta}{\partial x_j} = Q, \qquad (1.5)$$

where θ is a general scalar, and Q is a source term.

1.2.3 Direct Numerical Simulation

Direct Numerical Simulation (DNS) involves solving the governing equations describing the transport of momentum and scalar quantities in the atmospheric boundary layer with a computational grid fine enough to resolve the smallest turbulent length scales [44]. Direct numerical simulation (when applicable) is the simplest modeling approach, where any inaccuracies in the solution lie in the equations themselves, boundary conditions or in the numerical solution, as all terms in the governing equations can be explicitly calculated. This can provide valuable insight into the turbulent flow field, as the turbulence is directly calculated instead of modeled.

DNS is not generally used in the study of the ABL or plant canopies because of the large computational cost associated with the fine grid requirements. To perform DNS of a 1 km^3 turbulent ABL, it would require on the order of 10^{18} grid points to resolve the smallest turbulent length scales. A simulation at this grid resolution is not feasible with current computational resources, as computational time would be on the order of years. In the future (i.e., 30-50 years), if computational capabilities continue to increase as expected, it may be possible to use DNS as a tool in studying the atmospheric boundary layer [65].

1.2.4 Reynolds-Averaged Navier Stokes

Another popular method for simulating turbulent flows is to solve the Reynolds equations for the mean variables. This method is commonly called Reynolds-Averaged Navier Stokes or RANS [44]. The Reynolds equations are obtained by decomposing the total velocity into a mean and fluctuating component,

$$u_i = \overline{u_i} + u_i',$$
(1.6)

and similarly for scalar variables,

$$\theta = \overline{\theta} + \theta',$$
(1.7)

where an over-bar represents the mean component, and a prime represents the fluctuating component. When this representation of the turbulent field is substituted into eqns. 1.2 and 1.4, the following Reynolds equations are obtained

$$\frac{\partial \overline{u_i}}{\partial x_i} = 0, \tag{1.8}$$

$$\frac{\partial \overline{u_i}}{\partial t} + \frac{\partial \overline{u_i u_j}}{\partial x_j} = -\frac{\partial \overline{p}}{\partial x_i} - \frac{\partial \overline{u_i' u_j'}}{\partial x_j} + F_i. \tag{1.9}$$

The resulting Reynolds equations are similar to the previous equations, but now the dependent variables are mean quantities and a new term on the RHS of eqn 1.9 presents itself. This term, commonly referred to as the Reynolds stress term, represents all of the effects of turbulence. Unfortunately, there is no known equation to calculate this term, which results in an equation set that cannot be solved. In order to solve this set of equations, the Reynolds stress term must be modeled.

The Reynolds stresses are generally modeled either using the turbulent-viscosity hypothesis or by directly solving modeled transport equations for the Reynolds-stress [44]. The turbulent-viscosity hypothesis states that the Reynolds stress is proportional to the mean strain rate,

$$-\overline{u_i u_j} = 2\nu_T \overline{S_{ij}}, \tag{1.10}$$

where $\overline{S_{ij}} = \frac{1}{2} \left(\frac{\partial \overline{u_i}}{\partial x_j} + \frac{\partial \overline{u_j}}{\partial x_i} \right)$, ν_T is referred to as the turbulent viscosity or eddy viscosity. With the specification of ν_T, the Reynolds equations become a closed set of equations that can be solved for the mean velocity field. There have been a wide variety of models proposed to calculate ν_T, ranging in complexity from algebraic models to differential transport equations for turbulence quantities (see Wilcox 2006 [69]).

As previously mentioned, the Reynolds stress term may also be calculated by solving a transport equation for each Reynolds stress component, $\overline{u_i' u_j'}$, and a turbulence quantity that provides a length or time scale (such as dissipation rate ε.) This type of model has a better level of description and completeness than turbulent-viscosity models, but also significantly increased computational cost.

Similarly, this approach can be applied to eqn. 1.5, which results in the mean scalar equation

$$\frac{\partial \overline{\theta}}{\partial t} + \frac{\partial \overline{u_j}\overline{\theta}}{\partial x_j} = -\frac{\partial \overline{u_j'\theta'}}{\partial x_j}, \tag{1.11}$$

where averaging results in a similar RHS term, commonly called the scalar flux, which accounts for all turbulence in the scalar field. This term is generally modeled according to the gradient-diffusion hypothesis, which states that the scalar flux is transported down the mean scalar gradient [44]. According to this hypothesis, the scalar flux is calculated as

$$\overline{u_j'\theta'} = -D_T \frac{\partial \overline{\theta}}{\partial x_j}, \tag{1.12}$$

where D_T is the turbulent diffusivity.

RANS has been reliably used to model the ABL for nearly 40 years. This method offers significant cost savings over DNS because of its much looser resolution requirements. However, since all turbulence is modeled, the choice of such turbulence models can greatly influence simulation results. Initially, efforts were directed towards modeling buoyancy-driven atmospheric surface layer flows. Several models were proposed that used second-order closure models that assume simple gradient transport for third-order fluxes [27, 77, 76]. Zeman and Lumley [80] proposed a model that better simulates buoyancy-driven flows by including buoyancy-turbulence interactions. Mellor and Yamada [35] proposed a model that can be applied to a wide variety of engineering and geophysical flows that compared well with numerous experimental data sets. More recently, RANS closure models have been proposed that are able to simulate vegetative flows. Wilson and Shaw [71] first proposed a one-dimensional model that neglected buoyancy effects for flow within vegetative canopies. Finnigan [15] and Raupach et al. [48] proposed models that used volume averaging instead of horizontal averaging, and many models have since been proposed that use various other types of averaging [29, 66].

Canopy flows present problems inherent in RANS modeling. One of the most important problems with all RANS modeling is the fact that only mean variables are obtained and all turbulence is modeled. This means that the solution gives no insight into the turbulence, and results are entirely dependent on the chosen model. In the canopy, turbulence is dominated by large, intermittent structures with length

scales on the order of the canopy height [16]. The intermittency of the canopy is not captured by RANS simulations, which is a difficult feature to capture for any local closure model [54]. Since transport is dominated by large-scale coherent structures [16], the assumption that transport is a diffusion process is generally not accurate. Recently, other methods of turbulent canopy flow simulation have gained popularity which, in general, better model these types of flows.

1.2.5 Large-Eddy Simulation

Large-eddy simulation (LES) is a method for simulating turbulent flows that has become popular among researchers over the last few decades [13, 6, 37, 54, 42]. LES is a compromise between DNS and RANS in that it achieves some of the accuracy of DNS by resolving a significant percentage of the turbulence, and some of the cost savings of RANS by modeling the unresolved turbulence. In LES, the velocity (and other variables) are separated into a resolved and filtered component

$$u_i = \widetilde{u_i} + u_i',$$

(1.13)

where the tilde denotes the resolved component and the prime denotes the filtered component. The resolved component is found by applying a low-pass filter to the velocity field, which results in a field with characteristic turbulent length scales larger than the filter width, Δ. The filtered component, which is presumably less important, is modeled. When the filter is applied to eqns. 1.2, 1.4 and 1.5 we obtain

$$\frac{\partial \widetilde{u_i}}{\partial x_i} = 0,$$

(1.14)

$$\frac{\partial \widetilde{u_i}}{\partial t} + \frac{\partial \widetilde{u_i}\widetilde{u_j}}{\partial x_j} = -\frac{\partial \widetilde{p}}{\partial x_i} - \frac{\partial \tau_{ij}}{\partial x_j} + F_i,$$

(1.15)

$$\frac{\partial \widetilde{\theta}}{\partial t} + \frac{\partial \widetilde{u_j}\widetilde{\theta}}{\partial x_j} = -\frac{\partial q_i}{\partial x_j}.$$

(1.16)

The effects of the subfilter scales (SFS) on the dependent variables appear in the SFS stress and flux terms, τ_{ij} and q_i, respectively. These terms are defined as

$$\tau_{ij} = \widetilde{\tilde{u}_i \tilde{u}_j} - \tilde{u}_i \tilde{u}_j \quad \text{and} \tag{1.17}$$

$$q_i = \widetilde{\tilde{u}_i \tilde{\theta}} - \tilde{u}_i \tilde{\theta}. \tag{1.18}$$

There are no known equations to directly calculate the SFS stress and flux, therefore they must be modeled using information from the resolved variables. There is more flexibility in the formulation of SFS models for LES than RANS due to the fact that a large portion of the turbulence is resolved. The SFS model is most important near walls or any high shear region, where the fraction of unresolved energy to total energy is relatively large [46].

There have been numerous SFS models proposed, with the most common being eddy-viscosity/eddy-diffusivity models [37], similar to those previously discussed for RANS (see eqns. 1.10 and 1.12). As with RANS, there have been numerous methods proposed for modeling ν_T and D_T, each with varying applicability and complexity [57, 30, 13, 6, 19].

Large-eddy simulation was originally developed for meteorological applications [57], and has since become a popular tool for studying the ABL. LES later developed into a reliable tool for studying turbulence, where most researchers using LES were interested in either geophysical or engineering flows. The earlier work in LES was done studying simpler wall-bounded channel flows with the assumption of isotropic turbulence [39, 43], with hopes that it could be applied to complex engineering flows in the future. LES has since become the state-of-the-art tool in studying turbulent flows [44].

LES has been applied to atmospheric canopy flows by a wide range of researchers. Shaw and Schumann [54] performed LES of a forest canopy, where the canopy was modeled as a porous drag source/sink. Patton et al. [42] simulated flow in wheat canopy with intermittent windbreaks protruding from the top of the vegetation in a similar manner. Due to limited resolution, the vast majority of researchers have treated the vegetative canopy as a porous drag source, as Shaw and Schumann did [42, 55, 79].

Because of its strength in atmospheric canopy flows, the author has chosen to use LES in the study of flow in and around grape vineyards. LES is able to resolve large

flow structures characteristic of canopy flows. Since much of the flow is resolved, this will also allow for more flexibility when choosing particle dispersion models. Furthermore, the intermittency of the canopy turbulence is captured in the LES, which presumably plays a significant role in particle transport.

1.3   Modeling Particle Transport

Many researchers interested in atmospheric flows are also interested in how particles (i.e., tracers, pollutants, microorganisms, etc.) that are released into the atmosphere will be transported by the turbulent wind field. In this research, the interest is focused toward the transport of fungal pathogens in vegetative canopy flows. There are many ways of modeling particle transport, but any type of model relies on the fact that there is some information about the velocity field. With that information, it can then be determined how particles are transported through the use of a transport model.

The transport of particles may be viewed from two types of reference frames: Lagrangian or Eulerian. Some researchers have chosen to study particle transport from a fixed, or Eulerian reference frame [28, 3, 11]. Generally in this approach a transport equation is solved for particle concentration throughout the domain. For turbulent dispersion, this leads to a term which must be modeled due to the nonlinear advection term (similar to eqn.1.9). One advantage to this method is that the mean velocity can be obtained via relatively simple parameterizations, and the turbulence effects can be modeled using K-theory [3]. This leads to a method that can obtain relatively realistic results in areas sufficiently far from the source and with low turbulence intensity [71]. An arguably better way of understanding particle dispersion is from a Lagrangian framework where individual particle trajectories are followed [23, 62, 4, 58, 67, 9]. When modeling particle transport in this framework, particles are assumed to be passive tracers that move with fluid elements, and whose positions can be calculated in terms of the velocity field that transports them

$$\frac{dx_i}{dt} = u_i, \tag{1.19}$$

where x_i and u_i are particle position and velocity in each Cartesian direction at

any instant. This is a good assumption for flows with a sufficiently large Reynolds number, where molecular diffusion of the ensemble mean concentration is very small. Furthermore, it has been assumed that the drag force acting on particles is negligible, which is generally true for particles with diameters smaller that 100 μm (modeled particles are about 30 μm in diameter.) In complex flows where techniques such as similarity theory (as proposed by Taylor in 1921 [63]) are not valid, Lagrangian models tend to be much better suited for these types of problems, particularly complex atmospheric flows [62]. They can be applied to a wider variety of situations, such as non-Gaussian, inhomogeneous, unsteady turbulence.

Since large-eddy simulation was chosen as the primary tool for canopy modeling, determining the total Lagrangian velocity that transports the particles is non-trivial. Recall that the LES solution provides only the *resolved* velocity component. Since the Lagrangian transport equation requires the total velocity, the unresolved portion of the velocity must be modeled. Gopalakrishan and Avissar [21] argued that there is no proper treatment for the SFS particle velocity, and thus they calculated particle trajectories based only on the resolved velocity. The majority of researchers to date have chosen to implement stochastic or random-walk models for the SFS particle velocity [51, 58, 67, 25, 10]. Particles are assumed to behave in a Markovian or "memory-less" manner. This is a reasonable assumption for large Reynolds number flows like the ABL because particles are generally not autocorrelated over time scales larger than the Kolmogorov time scale [40]. As long as the interval for calculating particle trajectories, Δt, is much larger than the Kolmogorov time scale, this assumption is generally reasonable. This concept was first applied to dispersion in canopies by Wilson et al. in 1981 [72, 73, 74]. In 1987, Thomson [62] suggested a general stochastic differential equation for the total Lagrangian velocity from which random-walk models can be formulated. He also suggested the well-mixed criterion, which all models should satisfy. The well-mixed criterion states that an initially well-mixed cloud of particles must remain well-mixed. The difficulty of Thomson's formulation is that a unique solution cannot be found that satisfies his equation and also satisfies the well-mixed criterion. Some particular solutions have been proposed, but each of these models produce nontrivially different results for the same input velocity [7]. Many

other models have been proposed which compare well to experimental data, but do no necessarily apply to general cases (i.e., inhomogeneous, anisotropic, or non-Gaussian turbulence) [31, 22, 8, 67, 10].

1.3.1   Particle Deposition

As spores travel through a canopy, some will come in contact with vegetative elements (leaves, branches, trunks, etc.). Of those spores, some will deflect off of the vegetation and back into the air, while some will become deposited onto vegetation elements. Deposited spores may be released back into the air if local wind conditions cause them to detach from the vegetation. This complex phenomenon poses great difficulty when attempting to implement numerical models. It is not possible to explicitly determine whether particles impact the canopy because it is not currently possible to explicitly resolve all canopy elements. Instead, a model is used that will hopefully accurately represent the deposition process *on average.* The formulation of such statistical deposition models can be a difficult task. When this process is closely examined, there are a seemingly endless number of variables to account for that can impact deposition. Such possible variables are temperature, humidity, leaf flutter, particle size/mass, presence of wake regions, vegetation surface texture, to name a few. There are also other objects in the canopy that can remove particles such as weeds, dead vegetation, cobwebs, etc.

Although the problem is generally considered to be unsolved (and potentially un-solvable), there have been many researchers who have attempted to formulate models for deposition of particles on vegetation. Those who view particle dispersion from an Eulerian framework generally derive a differential equation that causes the canopy to act as a sink for particle concentration in a similar manner as the canopy acts as a sink for momentum [56, 50, 68]. These formulations generally rely on accurate specification of the deposition velocity, which for particle sizes on the order of microns can be uncertain by an order of magnitude or more [56]. Another type of deposition model, generally referred to as "ballistic" models, involve using simple parameterizations based on how far particles travel on average before they are deposited [41]. Ballistic models may be able to replicate bulk statistics to some degree; however, they are not

likely to provide accurate distributions of deposited particles in the canopy. Results are also entirely dependent on the parameterization choice. A third type of model involves calculating the probability of particle deposition at discrete time intervals. Legg and Powell [28] proposed a model of this type that calculated the probability of deposition as the sum of the probability of deposition due to horizontal impaction and the probability of deposition due to vertical settling. Each term is based on relatively well-studied concepts of particle impaction on cylinders, where the vertical term assumes that all particles that settle onto the foliage by sedimentation adhere to the surface [33, 52, 75]. Aylor [2] improved this model by determining an equation for the efficiency of impaction by fitting to experimental data for vertical cylinders.

CHAPTER 2

NUMERICAL MODELS

2.1   LES Subfilter Scale Model

As previously discussed, large-eddy simulation has been chosen to model the turbulent atmospheric boundary layer. The filtered Navier-Stokes equations, as written in eqns. 1.14, 1.15 and 1.16, are assumed to exactly represent the turbulent flow field. However, these do not represent a closed equation set, and therefore the SFS stress and flux terms must be modeled. The model choice is an important factor in how accurately the LES solution represents the actual flow, particularly at the sub-filter scale [36].

An eddy viscosity model has been chosen to parametrize the SFS stresses and fluxes. This model states that the deviatoric component of the SFS stress is proportional to the filtered velocity gradients, and the SFS flux is proportional to the scalar gradients, or

$$\tau_{ij} - \frac{1}{3}\tau_{kk}\delta_{ij} = -2\nu_T\widetilde{S_{ij}}, \tag{2.1}$$

$$q_i = -D_T\frac{\partial\tilde{\theta}}{\partial x_i}, \tag{2.2}$$

where ν_T is the eddy-viscosity, $\widetilde{S_{ij}} = \frac{1}{2}\left(\frac{\partial\tilde{u}_i}{\partial x_j} + \frac{\partial\tilde{u}_j}{\partial u_i}\right)$ is the filtered strain-rate tensor, and D_T is the eddy-diffusivity.

With the specification of ν_T and D_T, a closed equation set is obtained. The eddy viscosity, ν_T, has been specified as the product of a characteristic length and velocity scale

$$\nu_T = (C_s\Delta)^2|\widetilde{S}|, \tag{2.3}$$

where $C_s\Delta$ is a length scale and $|\widetilde{S}| = \widetilde{S_{ij}}\widetilde{S_{ij}}$. C_s is referred to as the Smagorinsky coefficient, named after Joseph Smagorinsky who first proposed the model in 1963

[57]. The eddy-diffusivity can be related to the eddy-viscosity via the SFS Schmidt number, which can be used to write a model for the eddy-diffusivity as

$$D_T = (C_s \Delta)^2 \, Sc_{sfs}^{-1} |\widetilde{S}|, \qquad (2.4)$$

where $Sc_{sfs} = D_T / \nu_T$.

Although ν_T and D_T has now been specified, C_s and Sc_{sfs}^{-1} must also be specified to complete the turbulence closure. The simplest model for C_s and Sc_{sfs}^{-1} is to specify them as constants [30]. This approach performs well only for simplified isotropic cases, but performs poorly for anisotropic cases such as in the ABL [59]. This also assumes that some information about the flow is available prior to the simulation that helps choose reasonable values for C_s and Sc_{sfs}^{-1}.

Germano [19] proposed a model in which the SFS coefficients are dynamically optimized instead of specified a priori. In this study, the model proposed by Portè-Agel et al. [45] is used which does not neglect scale dependence (which was neglected by Germano) and uses Lagrangian averaging. This model has been well validated in cases of neutrally stratified flow as well as buoyancy driven flows [59, 60].

2.1.1 Representation of the Canopy

Because of limited resolution, the canopy is modeled as a semi-continuous volume which exerts a drag force on the flow, as done by Shaw and Schumann [53]. This is done by adding a drag force term to the RHS of the conservation of momentum equations

$$\frac{\partial \widetilde{u}_i}{\partial t} + \frac{\partial \widetilde{u}_i \widetilde{u}_j}{\partial x_j} = -\frac{\partial \widetilde{p}}{\partial x_i} - \frac{\partial \tau_{ij}}{\partial x_j} + F_i + D_i, \qquad (2.5)$$

$$D_i = c_d \, a \, \widetilde{u}_i \, \widetilde{V}, \qquad (2.6)$$

where c_d is the drag coefficient, a is the local leaf area density, $\widetilde{u}_i$ is the resolved velocity component, and $\widetilde{V}$ is scalar wind speed. The leaf area density is defined as the leaf surface area per canopy volume, and is generally determined experimentally. An integrated measure of leaf density is the leaf area index (LAI) which is defined as

$$LAI = \int_0^H a(z)\,\mathrm{d}z, \tag{2.7}$$

where H is canopy height, a is leaf area density (m^2/m^3), and z is vertical position.

2.2 Lagrangian Particle Dispersion Model

There are many methods for treating the SFS particle velocity, ranging from neglecting it, to complex stochastic models. In the following chapters, simulation results will be shown for several commonly used models and how these models improve results over the "no-model" formulation.

2.2.1 Variance Model

The addition of a stochastic SFS velocity model generally should at the very least improve results by improving the level of mixing achieved in the flow. Perhaps the simplest version of a Lagrangian stochastic model is when the SFS particle velocity is modeled as a random number scaled by some characteristic function. This can be represented by

$$u_i' = f_i(x, y, z)\eta, \tag{2.8}$$

where $f_i(x, y, z)$ is some scaling function, and η is a Gaussian random number with a mean of zero and a standard deviation of one. The methods of Uliasz [64] have been followed which chooses $f_i(x, y, z)$ to be the velocity variance, σ_i. However, since only the resolved variance is available, the SFS particle velocity model can be written as

$$u_i' = \widetilde{\sigma}_i(z)\eta, \tag{2.9}$$

where $\widetilde{\sigma}_i(z)$ is the resolved velocity variance at each discrete horizontal level.

Because of the choice for η, it has been assumed that the turbulence below the filter scale is Gaussian, and since variances are calculated on horizontal planes, it has also been assumed that the turbulence is horizontally homogeneous. These are not good assumptions for many complex flows, particularly in a plant canopy. Vertical velocity distributions generally show inhomogeneity and nonzero skewness, with the vertical velocity skewness scaling as $Sk_w \sim \overline{w^3}/\sigma_w^3$ [18].

One obvious problem with this model is that since the resolved velocity is used, this model opposes reality as resolution is increased/decreased. As resolution is increased, the flow becomes better resolved, and as a result the SFS component of the velocity should tend toward zero. With this model, the SFS velocity becomes larger as the flow becomes better resolved. Granted there is a stochastic component to the SFS velocity, this model does not exhibit the expected trends.

2.2.2 Langevin Equation Model

In 1987, Thomson [62] presented his general form stochastic differential equation for the Lagrangian velocity, which can be written as

$$\mathrm{d}u_{Li} = a_i \mathrm{d}t + b\mathrm{d}\xi_i, \tag{2.10}$$

where dt is the trajectory time step, ξ_i is an increment of a Weiner process that is uncorrelated in each direction, and a_i and b are functions to be determined.

In this research, the formulation of Weil et al. [67] has been adopted, who wrote eqn. 2.10 as

$$\mathrm{d}u_i' = \left(-\frac{f_s C_o \epsilon}{2} \lambda_{ik} u_k' + \frac{1}{2} \left(\lambda_{lj} \frac{\mathrm{d}\tau_{il}}{\mathrm{d}t} u_j' + \frac{\partial \tau_{il}}{\partial x_l} \right) \right) \mathrm{d}t + (f_s C_o \epsilon)^{1/2} \mathrm{d}\xi_i, \tag{2.11}$$

where C_o is a model constant (4 ± 2 [62]), ϵ is the turbulence dissipation rate, τ_{ij} is the SFS stress tensor, λ_{ij} is the inverse of the SFS stress tensor, and f_s is defined as

$$f_s = \frac{\langle e_s \rangle}{\langle e_s \rangle + \langle e_r \rangle}, \tag{2.12}$$

where $\langle e_s \rangle$ and $\langle e_r \rangle$ are the SFS and resolved turbulent kinetic energy averaged over horizontal planes, respectively. The first term in eqn. 2.11 is deterministic and accounts for the drift of the particle. The second term is a stochastic forcing term that reflects the random-like motions of particles in response to turbulent fluctuations.

Equation 2.11 can be applied in cases of inhomogeneous, anisotropic, Gaussian turbulence, with the assumption that the change in the resolved velocity, $\delta\tilde{u}_i$ is small during particle transport through a grid cell ($\delta\tilde{u}_i/\tilde{u}_i \ll 1$).

In cases of isotropic turbulence below the filter scale, the SFS stress tensor can be written as $\tau_{ij} = \delta_{ij}\sigma_s^2$, where $\sigma_s^2 = 2e_s/3$. With this substitution for τ_{ij}, eqn. 2.11 reduces to

$$\mathrm{d}u_i' = \left(-\frac{f_s C_o \epsilon}{2}\frac{u_i'}{\sigma_s^2} + \frac{1}{2}\left(\frac{1}{\sigma_s^2}\frac{\mathrm{d}\sigma_s^2}{\mathrm{d}t}u_j' + \frac{\partial\sigma_s^2}{\partial x_i}\right)\right)\mathrm{d}t + (f_s C_o \epsilon)^{1/2}\,\mathrm{d}\xi_i. \qquad (2.13)$$

Since a Smagorinsky model is used for the large-eddy simulation, there is no explicit calculation of the SFS TKE or dissipation. An approximation of e_s can be made by adopting the methods of Mason and Callen [32]

$$e_s = \frac{\left(\Delta C_s |\widetilde{S}|\right)^2}{0.3}, \qquad (2.14)$$

The turbulence dissipation rate is found by assuming that the ϵ is equal to the SGS dissipation rate (see eqn. 2.15.) This assumption is valid on average if the filter cutoff frequency lies in the inertial subrange.

$$\epsilon = \Pi = -\tau_{ij}\widetilde{S_{ij}} = -\frac{1}{2}\left(\Delta C_s\right)^2 |\widetilde{S}|^3. \qquad (2.15)$$

2.3 Foliage Deposition Model

As particles travel through a canopy, some particles impact canopy elements and will either become deposited or be reflected away. This effect may have an important effect on concentration gradients, especially for release heights less than the canopy height. Thus, a canopy deposition model has been implemented that will be compared to results where no model was used.

The methods of Aylor [2] have been followed, who formulated an equation for the probability of particle deposition over a time step, which can be written as

$$G^v = v_s f^x a E^x \mathrm{d}t + u f^z a E^z \mathrm{d}t, \qquad (2.16)$$

where v_s is the particle settling velocity, f^x and f^z are fractions of the plant area projected onto horizontal and vertical planes, u is the horizontal particle velocity, E^x and E^z are the efficiency of horizontal and vertical deposition, a is the plant area

density, and dt is the time step of particle trajectories. The first term represents the probability of deposition due to settling, and the second term represents the probability of deposition due to horizontal impaction.

The horizontal absorption efficiency, E^x, is assumed to be 1 [28, 2]. The vertical absorption efficiency, E^z, is calculated based on Aylor's fit to data for impaction to circular cylinders [2]

$$E^z = \frac{0.86}{1 + 0.442 \left(|u|\tau_R/L_v\right)^{-1.967}},\tag{2.17}$$

where L_v is the characteristic size of vegetation elements, and τ_R is the particle relaxation time which was calculated as $\tau_R = v_s/g$ [12]. To determine whether the particle is deposited, a random number, Z, is chosen from a uniform distribution between 0 and 1. If $G^v > Z$, the particle is indefinitely deposited and its position is no longer updated. If $G^v < Z$, the particle is unaffected and trajectory calculations continue.

CHAPTER 3

MODEL VALIDATION

3.1 Computational Code

Computer codes were developed to perform large-eddy simulations (LES) and Lagrangian particle dispersion simulations. They were created to implement the previously described numerical models in an accurate and efficient manner. These codes will be described in detail in the following two sections.

3.1.1 LES Code

A highly parallel code was developed in the FORTRAN language to perform large-eddy simulation of the turbulent canopy field. Because of the large computational cost of performing LES of the ABL, the code divides the workload amongst a large number of processors, each with their own separate memory. Processors transfer data amongst themselves when necessary via Message Passing Interface (MPI), which was developed at Argonne National Laboratories. The data is divided amongst processors into blocks that are continuous in the stream-wise (x) and vertical directions (z), and discontinuous in the span-wise (y) direction. Figure 3.1 shows one possible parallel configuration.

The code solves the filtered conservation of momentum and scalar concentration equations written in advective form

$$\frac{\partial \widetilde{u}_i}{\partial t} + \widetilde{u}_j \left(\frac{\partial \widetilde{u}_i}{\partial x_j} - \frac{\partial \widetilde{u}_j}{\partial x_i} \right) = -\frac{\partial \widetilde{p^*}}{\partial x_i} - \frac{\partial \tau_{ij}}{\partial x_j} + F_i + D_i, \tag{3.1}$$

where $\widetilde{p^*} = \widetilde{p} + \frac{1}{2}\widetilde{u}_i\widetilde{u}_j$ is the filtered dynamic pressure, and all other variables are as previously defined.

The domain is discretized into equally spaced intervals of spacing Δ_x, Δ_y, Δ_z. Equation 3.1 is discretized in the vertical direction using central finite-differences, which result in discretization errors of order $(\Delta_z)^2$. Derivatives in the horizontal
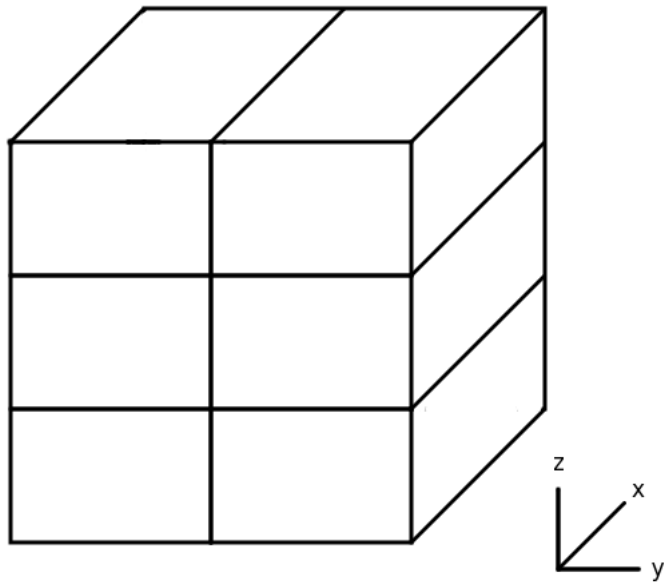
Figure 3.1. Possible parallelization scheme for LES code.

directions are calculated using pseudospectral methods, which generally result in discretization errors smaller than the order of $(\Delta_x)^6$ and $(\Delta_y)^6$. Equation 3.1 is integrated in time using an Adams-Bashforth scheme [14], which results in discretization errors of order $(\Delta_t)^2$. Calculations are done on a grid that is collocated in the horizontal direction, and staggered in the vertical direction. Calculation of $\widetilde{u_3}$ is done starting at $z = 0$, and calculation of $\widetilde{u_1}$, $\widetilde{u_2}$, and $\widetilde{p^*}$ is done starting at $z = \Delta_z/2$.

Filtering is done using a sharp spectral cutoff filter, which filters out length scales smaller than Δ, where $\Delta = (\Delta_x \Delta_y \Delta_z)^{1/3}$. Test filtering for the SFS model is done at scales of 2Δ and 4Δ, which is also done spectrally.

Horizontal boundaries are assumed periodic as required by the pseudospectral numerics used. The upper boundary condition is such that there is no stress/flux at the top of the domain, or $\partial \widetilde{u_1}/\partial x_3 = \partial \widetilde{u_2}/\partial x_3 = 0$. The value of τ_{i3} is needed lower boundary. These values are found by applying Monin-Obukhov similarity theory locally at every point on the surface [37, 32, 59]. The Monin-Obukhov similarity states that

$$U = \frac{u_*}{\kappa} \left[\ln \left(\frac{z}{z_o} \right) - \psi_M \right], \tag{3.2}$$

where u_* is the friction velocity, κ is the Von Karman constant $(= 0.4)$, z_o is the aerodynamic surface roughness height, and ψ_M is the stability correction for momentum [61]. Equation 3.2 is differentiated to calculate the magnitude of the vertical derivatives at lowest grid point. Vector decomposition is used to calculate the components in horizontal directions. This equation is also used to write the surface stress as

$$\tau_{i3} = - \left(\frac{\kappa}{\ln(z/z_o)} \right)^2 \tilde{u}_i M, \tag{3.3}$$

where $M = \sqrt{u_1^2 + u_2^2}$.

3.1.2   Lagrangian Particle Dispersion Code

A serial code was developed to simulate particle transport in the ABL. Three-dimensional fields of the required variables were output to file for the chosen Lagrangian dispersion model at evenly spaced time increments. These were then used to compute particle positions on a local machine using a single processor.

The code solves a differential equation for the position of each particle at each particle trajectory time step. If the particle time step is smaller than the time between the outputting of LES fields, linear interpolation was used between two successive LES files. Trilinear spatial interpolation was then used to calculate variable values within grid cells.

Because of the horizontal periodicity of the domain, trajectories for particles which travel beyond the horizontal boundaries of the domain can be calculated based on periodicity. Particles that travel above the vertical boundary of the domain were assumed to be lost and their positions were no longer calculated. This assumption may introduce a small amount of error in the results due to the fact that particles that rise above the domain height could potentially settle down and become deposited in the canopy at large downstream distances. Thus, it was assumed that the domain height is sufficiently large that an insignificant percentage of particles rise above the domain height.

For particles that hit the bottom of the domain, it was assumed that there were two possible outcomes: either the particle becomes indefinitely deposited on the ground or the particle deflects off of the ground and continues traveling. To determine which of these possibilities occurred, a stochastic model was used to predict the outcome. The vertical velocity, w, was compared to the settling velocity of the particle, v_s to determine the probability of ground deposition as follows

$$P_G = 2\frac{v_s}{v_s - w}; \qquad\qquad w < -v_s, \qquad\qquad (3.4\text{a})$$

$$P_G = 1; \qquad\qquad |w| < v_s. \qquad\qquad (3.4\text{b})$$

where P_G is the probability of deposition to the ground. To determine whether the particle is deposited, a random number, Z, is chosen from a uniform distribution between 0 and 1. If $P_G > Z$, the particle is indefinitely deposited and its position is no longer updated.

3.1.2.1 Rogue Trajectories

When using complex SFS velocity models, it is possible that the model can calculate physically unreasonable or "rogue" trajectories. For example, consider eqn.

2.13 when $\sigma_s^2 \ll 1$. The SFS variance is expected to be small in highly resolved areas of the flow, however, eqn. 2.13 predicts that the SFS velocity should be very large $(u_i' \to \infty)$ in these areas. Thus, some numerical limits must be imposed on particle trajectories to avoid such rogue trajectories [78].

Equation 2.12 can be used to impose limits on the SFS velocity. If $\langle e_s \rangle$ and $\langle e_r \rangle$ are replaced with u_{si} and u_{ri}, it can be said that

$$u_i' < \frac{f_s}{1 - f_s} \tilde{u}_i. \tag{3.5}$$

If this condition is not satisfied, the SFS velocity was chosen to be equal to the random forcing term in eqn. 2.11

$$u_i' = (f_s C_o \epsilon)^{1/2} \, \mathrm{d}\xi_i. \tag{3.6}$$

3.2 Model Validation: Highly Convective ABL

In 1974, Willis and Deardorff [70] published the results of an experiment to replicate particle dispersion in a convective planetary boundary layer. A Plexiglas tank was constructed and filled with water, where the bottom of the tank was uniformly heated to produce convection. The stability index $-z_i/L$ was approximately 100, which would classify the boundary layer as highly convective. An instantaneous line source of about 1150 neutrally buoyant oil droplets with an average diameter of 800 μm were released near the surface and allowed to travel through the tank. Particles were released at a height of 7% of the average boundary layer height. Photographs were taken in the Y-Z direction at various time intervals, which were processed to give particle distributions in the span-wise and vertical directions. This experiment proved to be very successful and has been highly referenced by researchers studying the convective ABL [35, 31, 67].

To validate the Lagrangian particle dispersion models, simulation results were compared against the experimental results of Willis and Deardorff. It was desired to replicate the concentration profiles obtained from this experiment using the LES and dispersion codes. The input parameters for the LES and dispersion simulations may be found in Appendix A.1.

Particle concentrations were sampled at discrete nondimensional times after release. The nondimensional time after release can be expressed as

$$X = \frac{w_*}{z_i}t, \tag{3.7}$$

where w_* is a convective velocity scale, z_i is the average boundary layer height, and t is time after release. The concentration of particles projected onto a square of area $\Delta_y \times \Delta_z$ is

$$c = \frac{n}{L_x \Delta_y \Delta_z}, \tag{3.8}$$

where n is the number of particles, L_x is the length of the domain in the stream-wise direction, and Δ_y and Δ_z are the grid spacings in the span-wise and vertical directions. The dimensionless concentration is defined as

$$C(X, Y, Z) = c(X, y, z)\frac{z_i^2 U}{S}, \tag{3.9}$$

where U is the average stream-wise velocity, S is the number of particles emitted per unit time, $Y = y/z_i$, and $Z = z/z_i$. The Y dependence of the dimensionless concentration can be eliminated by integrating eqn. 3.9 with respect to Y to yield the dimensionless cross-wind integrated concentration (CWIC)

$$\overline{C}^y = \int_{-\infty}^{\infty} C(X, Y, Z)\, \mathrm{d}Y. \tag{3.10}$$

Figure 3.2 shows model results of CWIC compared with the experimental results of Willis and Deardorff. Results show that the simulation is able to adequately predict particle concentration profiles for these stability conditions. All models were able to capture the elevated concentration maximum present at $X = 1.55$. Also note that the SFS velocity model used did not play a significant role in determining the shape of CWIC profiles. The difficulty in this validation case proved to be matching the conditions of the experiment and not the formulation an accurate SFS velocity model.

In much of the boundary layer, the fraction of SFS TKE to the total TKE (f_s) is relatively small, which is illustrated in Fig. 3.3. The SFS TKE fraction is relatively constant in most of the boundary layer, with its value being approximately 20%.
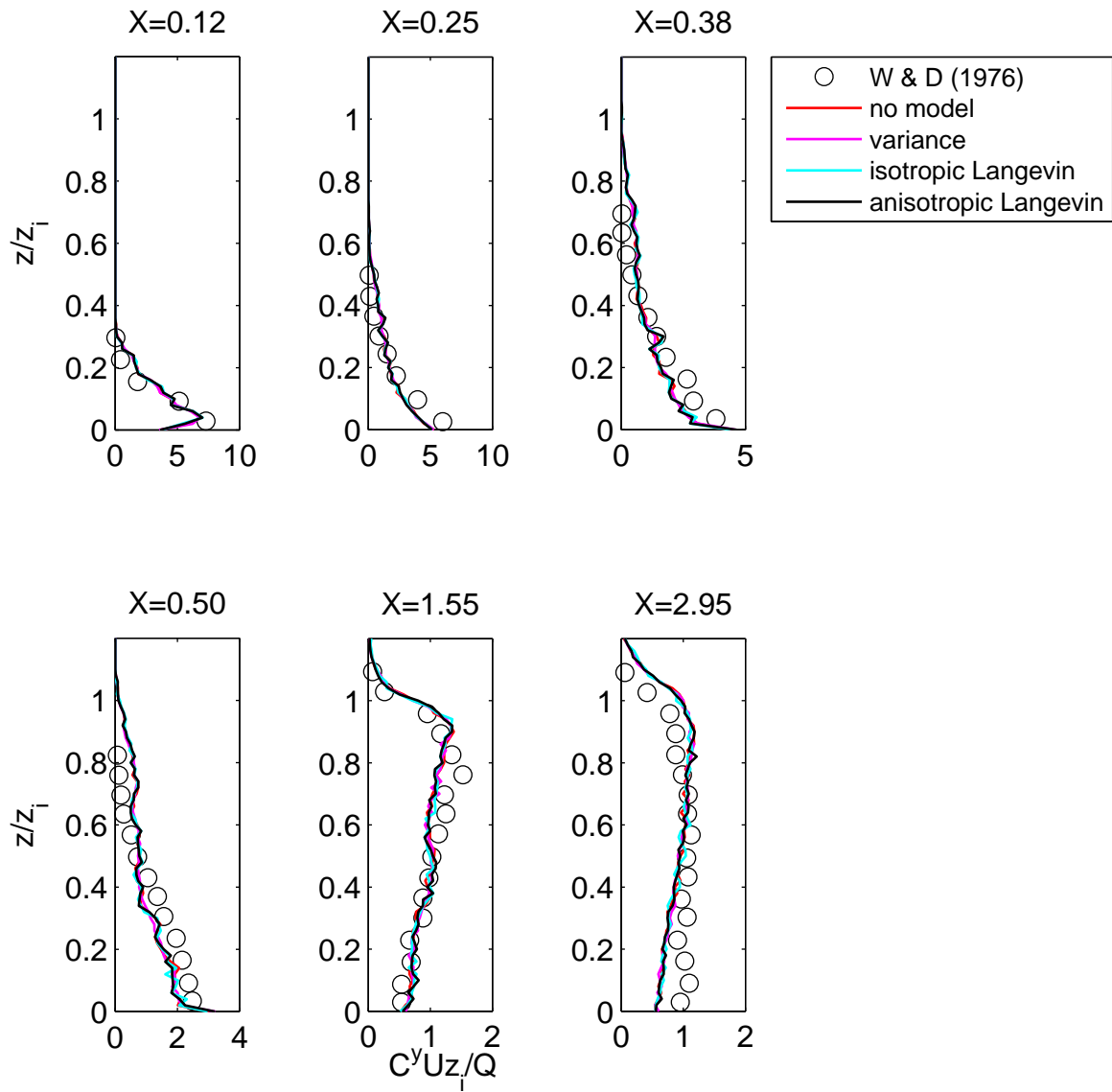
Figure 3.2. Comparison of CWIC vertical profiles for various model choices.
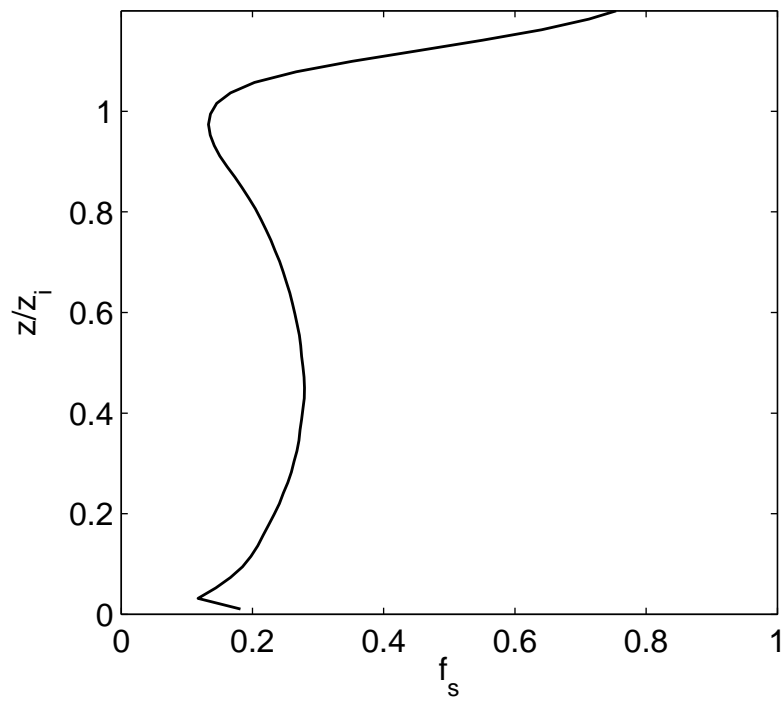
Figure 3.3. SFS TKE fraction for Willis and Deardorff validation case.

Thus the flow is fairly well resolved in these areas, and SFS particle velocity models are less important. As a result, SFS velocity model choice is generally less important in this flow than other more complex flows.

Near the surface, the SFS energy is much more important than in other areas of the flow because of the lack of resolution. In Fig. 3.4, the CWIC is plotted near the surface for various dimensionless times. The surface is defined as $0 < z < 0.067z_i$, which was the height of the lowest grid square in the Willis and Deardorff experiment. Even in the lowest grid square, the concentration showed little sensitivity to model choice. Although this case provides adequate validation for the general Lagrangian particle dispersion model, a more rigorous test of SFS velocity models is needed in which the SFS energy is large over a significant portion of the domain.

Weil et al. performed a similar validation study in which he compared the results of his SFS particle velocity model simulation (see eqn. 2.13) to the experimental results of Willis and Deardorff. Simulation results indicated that neglecting the SFS velocity tended to affect concentration results near the surface. This observation was not seen in the results previously presented in this study. Weil et al. uses a simpler eddy-viscosity model in their LES (see Moeng and Sullivan [38].) As a result, Weil et al. reports near-surface SFS TKE fractions nearly twice as high values shown in fig. 3.3. Thus, it is expected that SFS particle models will be more important near the surface, given the lack of resolution in the LES of Weil et al.

3.3   Model Validation: Spore Transport in a Wheat Canopy

A field experiment was performed by Aylor and Ferrandino [4] in which *Lycopodium* spores were released in a continuous wheat canopy. The canopy had a cumulative LAI of 3.0, the average wind speed based on the seven measurement locations was about 1.8 m/s, and the friction velocity, u_* was 0.35. Particles with an average diameter of about 30 μm were released at a height of 0.76 m in a 2.85 m tall wheat field. Spore traps were set up at various heights at a position of 4 m downwind of the release point. Wind speed was also measured at various heights using sensitive cup anemometers.

Measurements of the cumulative leaf area index (LAI) and cumulative stem area
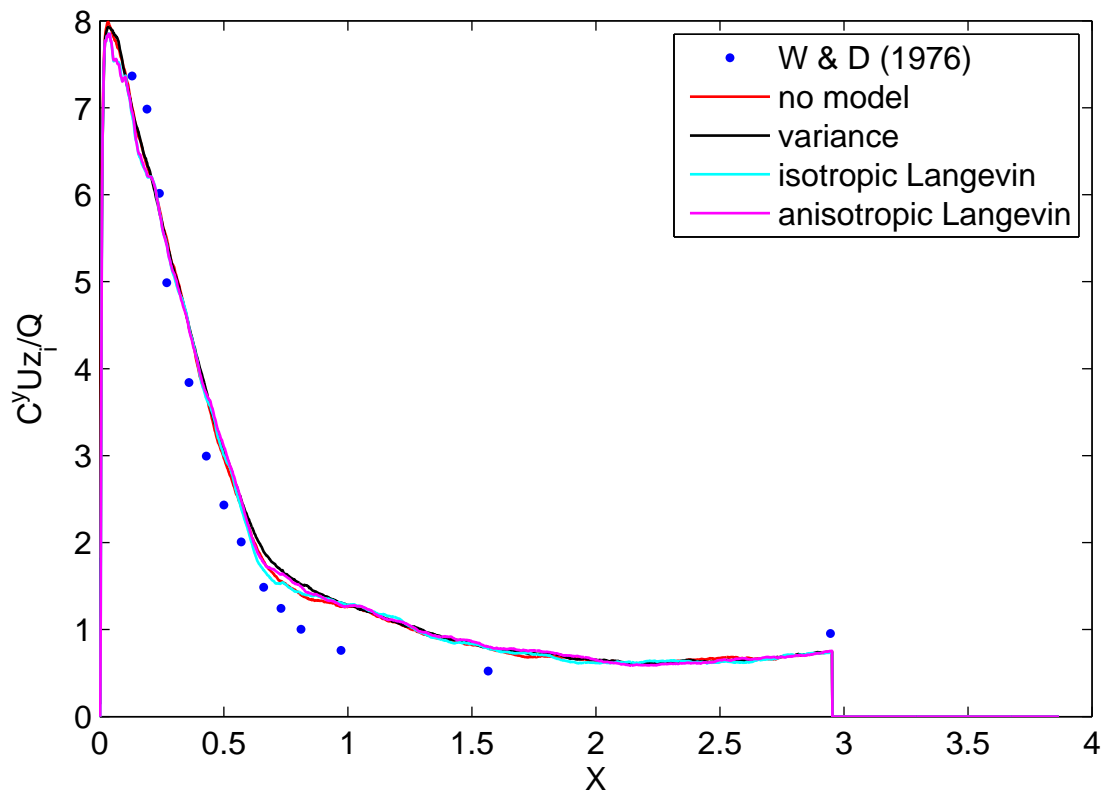
Figure 3.4. Comparison of CWIC surface values for various model choices.

index (SAI) are given for the wheat canopy. A third-order polynomial was fitted to the experimental data and differentiated to yield a profile for the leaf area density (LAD). As done by Aylor and Ferrandino, the SAI was assumed to vary linearly from 0 to 1 from z=0 to z=H, where H is the canopy height. When differentiated, this gave a constant stem area density profile of $dSAI/dz \approx 1.05$. The leaf and stem area density profiles were superposed, which yielded the profile used in the LES canopy model. This profile, as well as other important input parameters for the simulation are shown in Appendix A.2.

Figure 3.5 shows horizontal velocity and f_s profiles from LES of the wheat canopy. Given the LAI and SAI field measurements, the LES is able to accurately replicate the experimental velocity measurements of Aylor and Ferrandino. A drag coefficient of 0.75 was used to match the experimental velocity profile. C_d values are not reported by Aylor and Ferrandino, however a value of 0.5 was reported by Patton et al [42] for a simulated wheat canopy in a wind tunnel. For this case, the fraction of SFS kinetic energy to total kinetic energy (f_s) is much larger than in the convective ABL case. Inside the canopy, f_s is approximately 50% on average, with the largest values occurring near the surface. Above the canopy, f_s is slightly smaller yet still significant. This means that SFS particle velocity models will be more important in this case than the convective PBL case. Thus, this case is a more rigorous test of SFS particle velocity models.

3.3.1 Estimation of Dispersion Statistics

Aylor and Ferrandino used particle traps to deposit *Lycopodium* spores on microscope slides. A known volume of air was sampled, and any spores present in the volume of air were deposited on the slides. The number of deposited spores were counted to determine particle concentration at various heights.

In order to compare with the experimental data presented by Aylor and Ferrandino, a method must be formulated to calculate particle concentration and horizontal flux from the numerical data. For a release of N particles, the concentration of particles can be estimated by
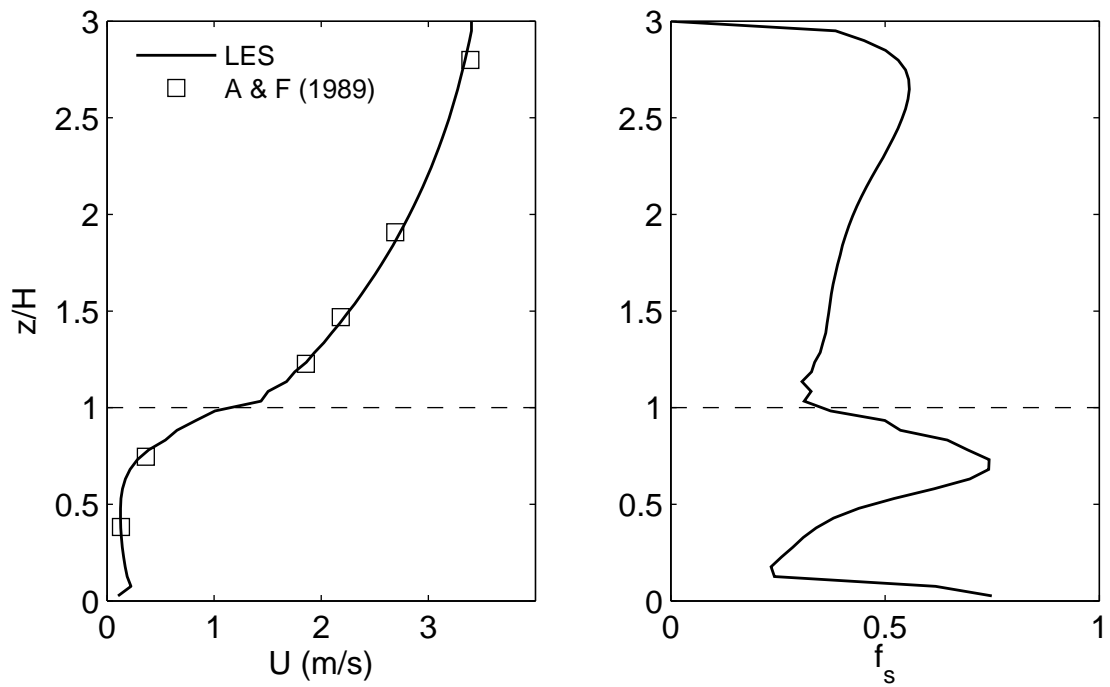
Figure 3.5. LES velocity statistics from Aylor and Ferrandino [4] validation case. Left Panel: Horizontal velocity. Right Panel: SFS TKE fraction.

$$C(x, z) = \frac{1}{T_s} \sum_{k=1}^{N} \frac{T_k}{V}, \qquad (3.11)$$

where T_s is the total simulation time, and T_k is the time that the kth particle remains in a volume V centered at the point (x, z).

The horizontal particle flux can be estimated by

$$F_x(x, z) = \frac{Q}{N \cdot l}(n^+ - n^-), \qquad (3.12)$$

where Q is the line source strength (spores $m^{-1}s^{-1}$), n^+ and n^- are the number of particles that cross a vertical line segment of length l in the positive and negative directions.

These methods will also be used in following sections to estimate particle concentrations and fluxes.

3.3.2 Model Comparison

Dispersion simulations were performed to attempt to replicate the Aylor and Ferrandino results for each available SFS velocity model. Particle release was performed in a similar manner as was done in the field experiment. Particles were released from six points along a 3.7 m line source. Concentration sampling volumes of size $\Delta_x \times 4\Delta_y \times \Delta_z$ were used to yield $C(x, z)$. The concentration was normalized by the release height, z_{os}, the average velocity, U, and the source strength, S, and plotted in Fig. 3.6.

Results show that models differ in their predictions more than was observed in the convective validation case. The "no model, "variance model, and "anisotropic model" predict similar particle concentration profiles. The isotropic assumption applied to Weil's formulation seemed to predict lower particle concentrations in the canopy. The similarity in particle models even in the case where the flow is unresolved indicates that possibly the stochastic forcing term in the Langevin equation dominates the model, and possibly neglecting SFS contributions to the velocity may be reasonable. However, the general anisotropic form of Weil's model is used in the simulations presented in the following sections. Such a model choice may be considered unjustified, other than the fact that the model may give marginally better results.
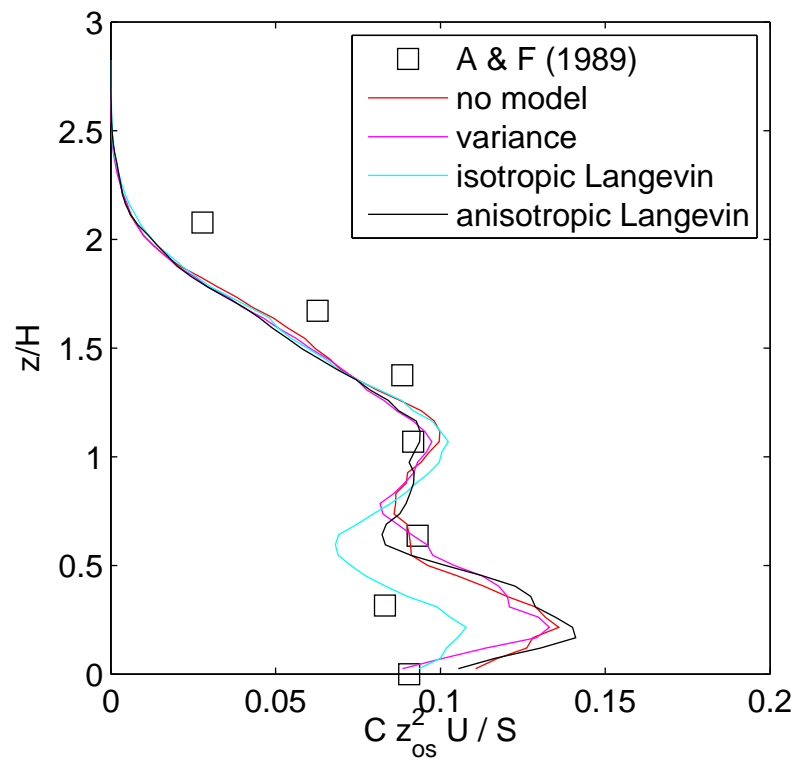
Figure 3.6. Concentration statistics from Aylor and Ferrandino [4] validation case.

Given the choice of the anisotropic form of Weil's model, the performance of this model will now be discussed. The validation study indicates a lack of mixing in the canopy, according to the experimental results. Based on the limited data provided by Aylor and Ferrandino, it is unclear whether this problem is a direct result of SFS particle velocity choice or whether the lack of mixing comes from damped turbulence in the LES results. Particle samplers in the field experiment were placed relatively near the release point. As the concentration profile is examined further downstream for simulation results, much higher mixing is observed. Hence, this indicates that models do not perform as well near particle sources.

CHAPTER 4

DISPERSION IN A GRAPE VINEYARD

The focus of this research was to simulate the transport of powdery mildew spores in grape vineyard canopies. This was accomplished using large-eddy simulation and the previously presented anisotropic Langevin equation model for particle transport. After validating these models with experimental data, these models were used as a predictive tool to examine how canopy geometry in grape vineyards affects powdery mildew dispersion.

4.1   Analysis of Dispersion in a Single Vineyard Geometry

A simulation was performed to examine velocity and dispersion statistics for a single vineyard geometry. The rows of the vineyard were oriented perpendicular to the mean wind. A line source of particles parallel to the rows was used to release particles at 75% of the canopy height. Particles are assumed to have a mean diameter of approximately 30 μm. The drift velocity of powdery mildew spores, v_s was assumed to be similar to the drift velocity of *Lycopodium* spores, which was about 0.02 m/s. In each simulation, 100,000 particles were released over a period of 5 minutes. It was determined that 100,000 particles was sufficient to obtain converged statistics. Figure 4.1 shows a general schematic of the simulated vineyard. The plants extend continuously in the direction normal to the page, and the rows repeat infinitely in the wind direction. The flow was driven by forcing the stream-wise velocity to have a mean value of 2 m/s. Based on the geometry of common vineyards, the row width was chosen to be 0.5 m, and the row height was chosen to be 2 m.

The majority of researchers who simulate row-oriented vegetation represent the canopy as a continuous volume and do not resolve the row structure [4, 54]. In this numerical experiment, the structure is sufficiently resolved to represent the spaces
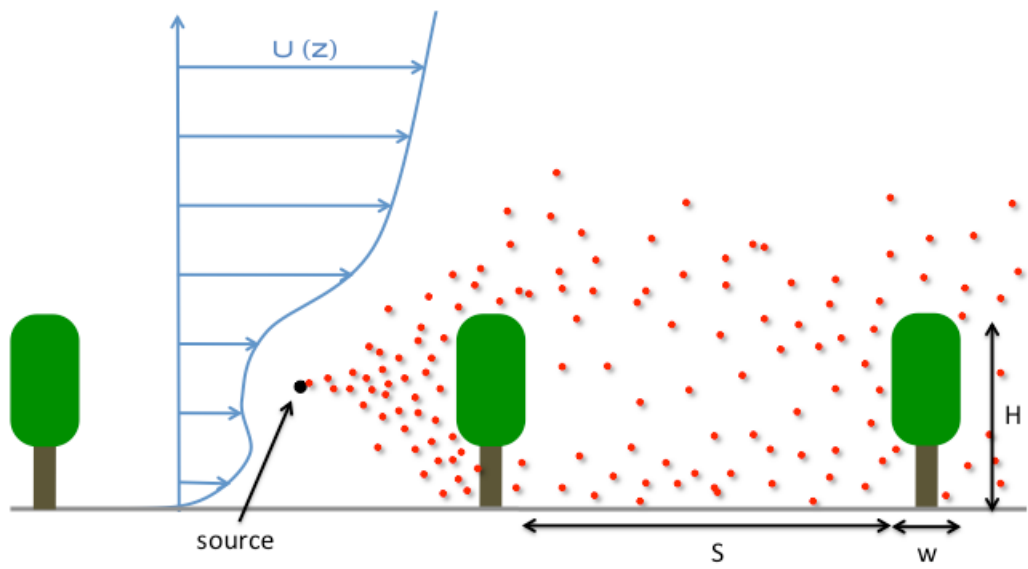
Figure 4.1. Particle release test case in a vineyard.

between vegetative rows. The grid resolution in the stream-wise direction, Δ_x, is approximately 0.2 m, which provides several grid points per row width.

For this experiment, values for leaf area index and row spacing were chosen to have values that might be observed in typical vineyards. The LAI was chosen to be 3.0 based on values reported by the Gladstone et al. 2003 data [20]. The LAI is defined as the leaf area index of a single row (excludes spaces between rows.) The shape of the leaf area density profile was chosen according to Gladstone's data for vertical shoot positioned trellis/training systems [20]. This shape was assumed to remain constant for different values of LAI, thus the profile was scaled to achieve the desired LAI. The row spacing was chosen to be 2.0 m based on values reported by the Johnson et al. 2003 data [24]. The row spacing is defined as the period of the rows (e.g., the center-to-center measurement of two adjacent rows.)
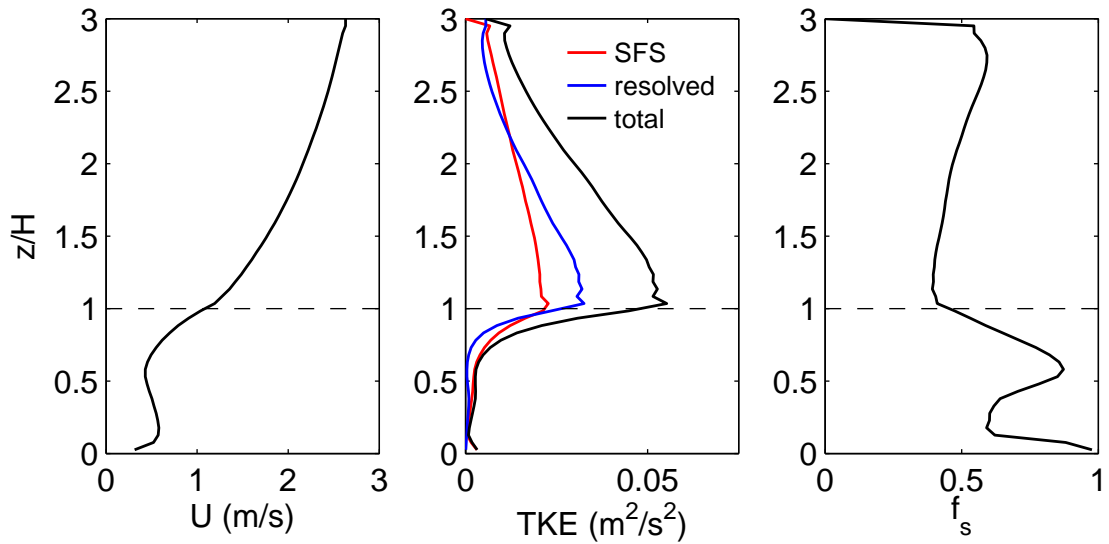
4.1.1 Velocity Statistics

Horizontally averaged statistics were calculated based on simulation data for the stream-wise velocity, turbulent kinetic energy, and f_s (see eqn. 2.12). Vertical profiles of these variables are shown in Fig. 4.2, which were time-averaged over a statistically steady period.

As expected, the classical *s-shaped* mean velocity profile is observed [54, 16]. A jet forms in the trunk space of the canopy due to the decreased drag of the trunks, which results in increased velocity in this region. The turbulent kinetic energy profile indicates that the total TKE is relatively small in the lower half of the canopy when compared with the rest of the domain. Although the total TKE is small, the unresolved contribution to the TKE is large, with values of f_s greater than 50%. This indicates that models for the SFS velocity will likely be important inside the canopy, as a significant portion of the scales of motion are unresolved. Even above the canopy, f_s is reasonable large, with values between 25% and 50%.

Since turbulence plays a large role in how particles disperse, it is useful to examine turbulence statistics in greater detail. Examining the correlation between u and w velocity fluctuations can provide valuable insight into canopy turbulence. Figure 4.3 shows velocity fluctuation vectors ($\vec{V} = \langle u', w' \rangle$) in the x-z plane for a portion of the vineyard. Vectors shown are spatially averaged in the span-wise direction and time

Figure 4.2. Vineyard simulation velocity statistics.
Left Panel: Stream-wise velocity. Middle Panel: Turbulent Kinetic Energy. Right
Panel: f_s. Dotted line indicates canopy top.
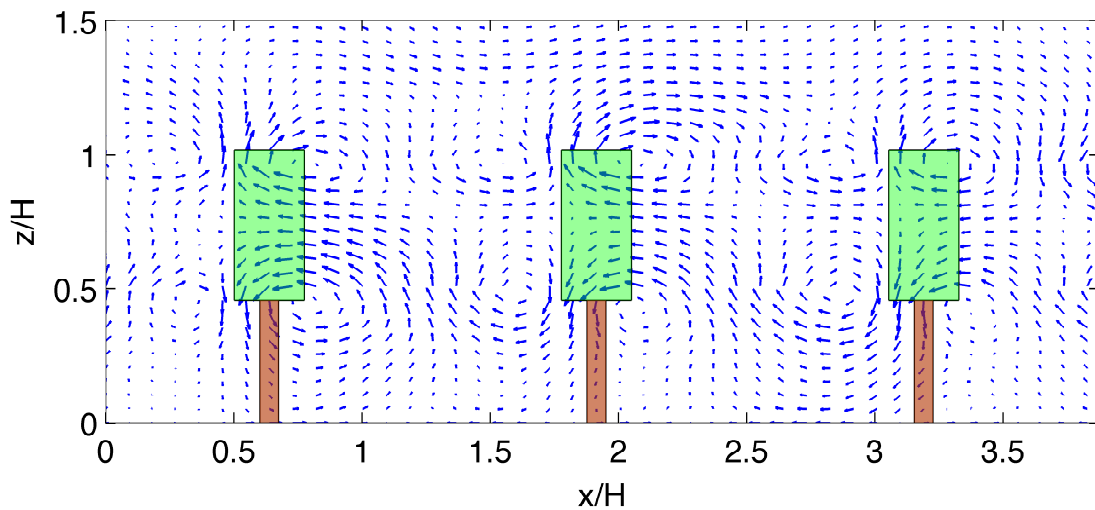
Figure 4.3. Velocity fluctuation vectors ($\vec{V} = \langle u', w' \rangle$) in the x-z plane. Mean flow
is from left to right.

averaged over a statistically steady period.

Results indicate that a periodic turbulence structure forms with a period equal to the row spacing. If vectors with negative u' and w' components are defined as sweep events, it can be observed that there is a high probability of sweep events in the area immediately upwind of the trunk space. Furthermore, if vectors with positive u' and w' components are defined as ejection events, it can be observed that there is a high probability of ejection events at the top of the vegetation of the canopy. Notice that the probability and magnitude of both sweep and ejection events begin to diminish in areas away from the plant rows.

Had the canopy been represented as a continuous volume of vegetation instead of resolving the row structure, this periodic sweep and ejection structure would not form in the same manner. This has the potential to significantly impact particle dispersion in the canopy, which will be examined more closely in later sections.

Another interesting feature of the row-oriented canopy is how the row structure influences vertical particle transport. Figure 4.4 shows a contour plot of the vertical velocity in the x-z plane for a portion of the vineyard. Vectors shown are spatially averaged in the span-wise direction and time averaged over a statistically steady period. Horizontally traveling particles which impact the upper third of row vegetation tend to be transported up and possibly out of the canopy by the increased vertical velocity at that location. Particles which impact the middle third of row vegetation have relatively low vertical velocity and tend to be transported straight through the vegetation. Particles that impact the lower third of row vegetation tend to be transported down and into the trunk space of the canopy by the increased downward velocity. This feature also suggests that resolving the row structure is important for vertical particle transport.

4.1.2 Dispersion Statistics

To understand how particles released from a line source within a vineyard canopy spread, particle dispersion statistics are first examined near the source. Figure 4.5 shows horizontal flux profiles for three downwind locations from the source. The profiles demonstrate that the flux profile is still approximately Gaussian after particles have crossed the first row. Further downstream, fluxes begin to decrease in areas of
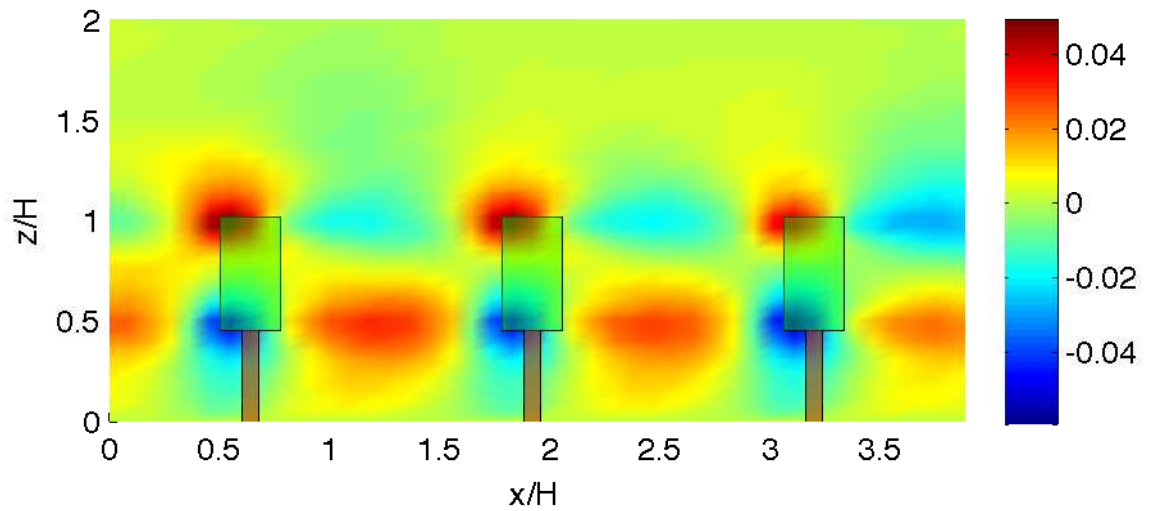
Figure 4.4. Mean vertical velocity magnitude (m/s) in the x-z plane. Mean flow is from left to right.
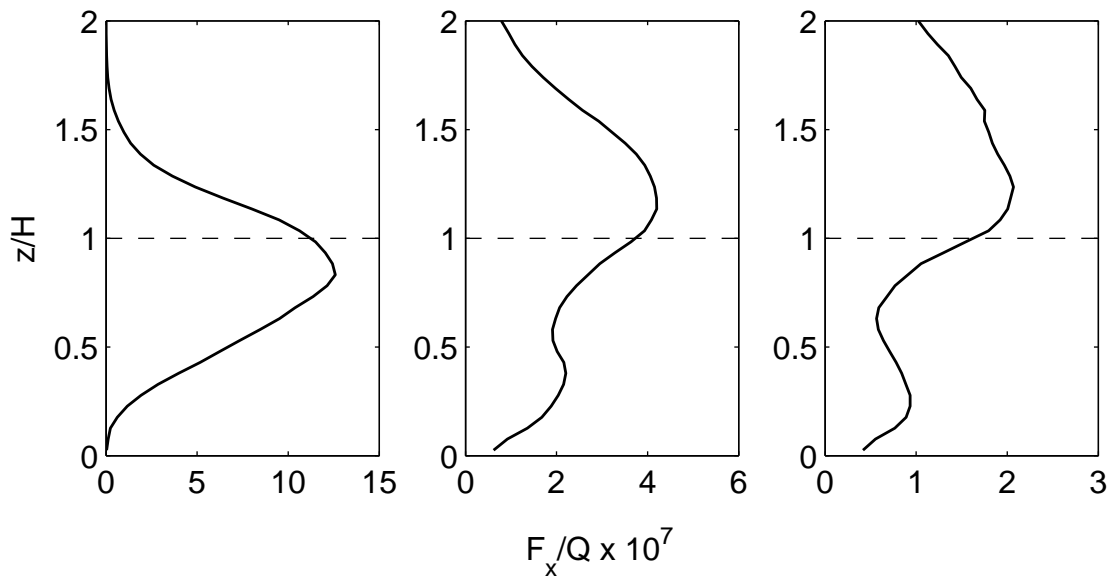
Figure 4.5. Horizontal particle flux at three downstream distances.
Left Panel: X = 2.5 m. Middle Panel: X = 8.0 m. Right Panel: X = 15.0 m.

high vegetation density due to the filtering effect of deposition. Fluxes become largest above the canopy where the velocity magnitude is largest and there is no vegetation on which particles can become deposited. Figure 4.6 shows a contour plot of particle concentration in the x-z plane for a portion of the vineyard. Concentrations are spatially averaged in the span-wise direction. The filtering effect of the vegetation can be clearly seen by the decreased particle concentrations in the wakes of vegetation.

4.1.3   Horizontally Continuous Representation of the Vineyard

Previously, a hypothesis was made that resolving the row structures in numerical simulations of grape vineyards is important in accurately predicting particle transport in the canopy. That hypothesis was tested by simulating an equivalent continuous canopy, where the LAI was decreased such that it had the same LAI as the discontinuous canopy with the spaces between rows taken into consideration. The "apparent" LAI, $\overline{LAI}$, of a continuous vineyard may be defined as

$$\overline{LAI} = LAI \left(\frac{V_r}{V_t} \right) = LAI \left(\frac{w}{w + s} \right), \tag{4.1}$$

where LAI is the leaf area index of the rows in the discontinuous canopy, V_r is the volume that the vegetation occupies in the discontinuous canopy, V_t is the total volume of the canopy including row spaces, w and s are row width and spacing, respectively (see Fig. 4.1.)

A simulation was performed which represented the canopy as a continuous volume of vegetation and had the same apparent LAI as the LAI=3.0 and spacing=2.0 case. The flow in each simulation was driven with an equivalent pressure gradient in the stream-wise direction. Furthermore, the same LAD profile was used in each case, and was scaled to obtain the desired LAI. Figure 4.7 shows a comparison of the horizontally averaged stream-wise velocity profile for both cases. Results indicate that the mean streamwise velocity is insensitive to whether the canopy row structure is explicitly resolved. The streamwise velocity in Fig. 4.7 was averaged over horizontal planes and over a statistically stationary period, thus any inhomogeneous motions from the discontinuous row structure have been removed by the averaging operation. Thus, results indicate that mean horizontal wind statistics can be obtained without
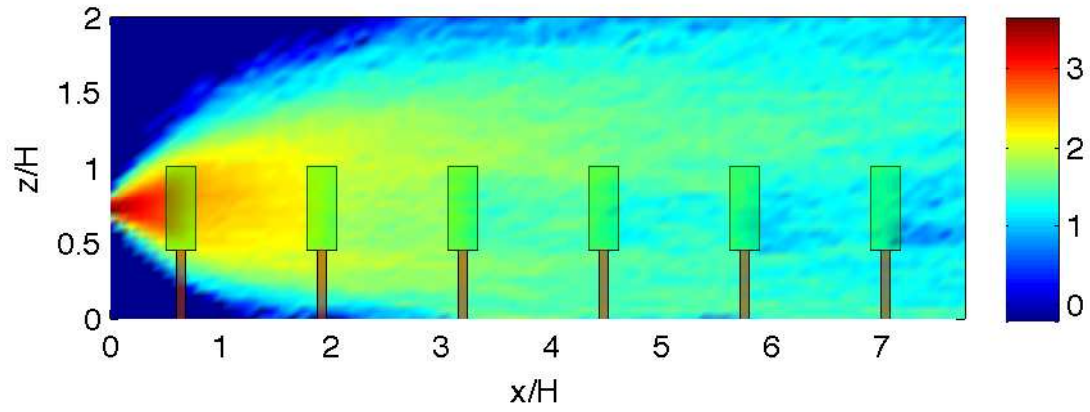
Figure 4.6. Particle concentration (m^{-3}) in the x-z plane. Mean flow is from left to right.
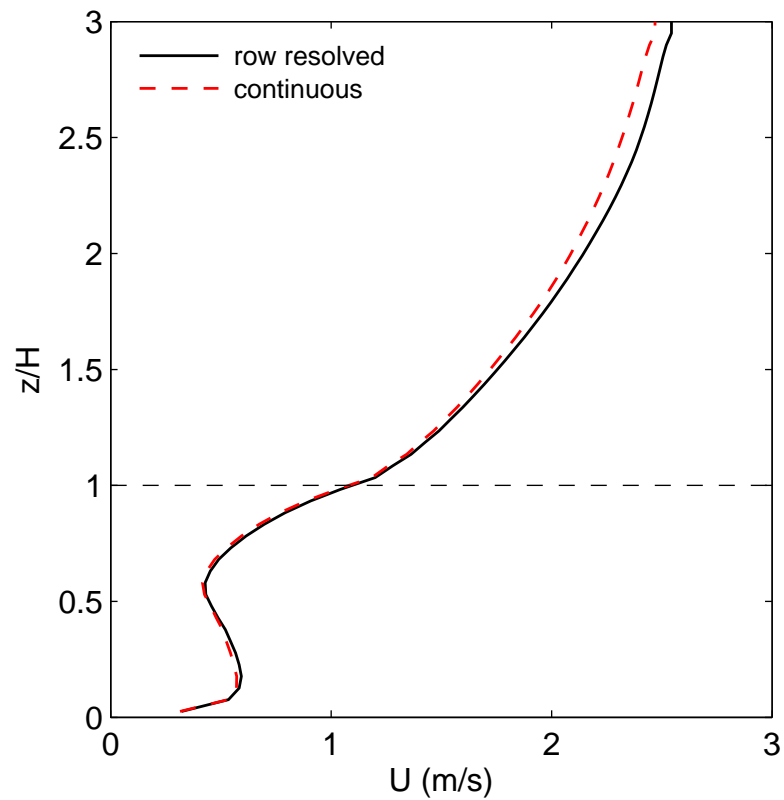
Figure 4.7. Stream-wise velocity comparison for continuous and row-resolved representations of the vineyard.

explicitly resolving canopy row structure for this specific geometry. However, as the canopy becomes less dense, or apparent LAI is decreased, resolving the row structure will likely become more important.

Any discrepancies between the continuous and discontinuous canopy representation will likely have an impact on particle dispersion. It is also likely that other dynamics such as sweep and ejection events that are not seen in spatially and temporally averaged statistics will cause differences in particle concentrations between the two cases. Figure 4.8 shows concentration profiles at three downstream distances from the release point for both types of canopy representation.

Results indicate that the continuous representation of the canopy overestimates particle concentration in the canopy, and underestimates concentration above the canopy. If a mean canopy concentration, C^*, is defined as

$$C^* = \frac{1}{H} \int_0^H C(z)\, \mathrm{d}z, \tag{4.2}$$

the downstream progression of concentration in the canopy can be compared for the continuous and row-resolved canopies (Fig. 4.9). Although differences are small, it appears that at distances greater than 4 m downstream of the release point, the concentration is higher within the canopy for the continuous vineyard representation, suggesting that there is less canopy escape.

This result may be further understood by examining the vertical particle flux at the top of the canopy. This flux gives a quantitative measure of particle escape from the canopy. The escape flux in the row-resolved case was 1.36×10^{-6} m^{-2}-t^{-1}, while the continuous case had a slightly smaller flux of 1.34×10^{-6} m^{-2}-t^{-1}. The higher escape flux in the row-resolved case leads to higher concentration above the canopy. Thus, representing the canopy as continuous not only results in increased particle advection, but particles are also less likely to be ejected out of the canopy. Furthermore, this result is also likely amplified in cases with smaller apparent LAI.

4.2 Comparison of Several Vineyard Geometries

The ability to limit the transport of powdery mildew spores from their source is of primary importance in limiting disease outbreaks in grape vineyards. Presumably,
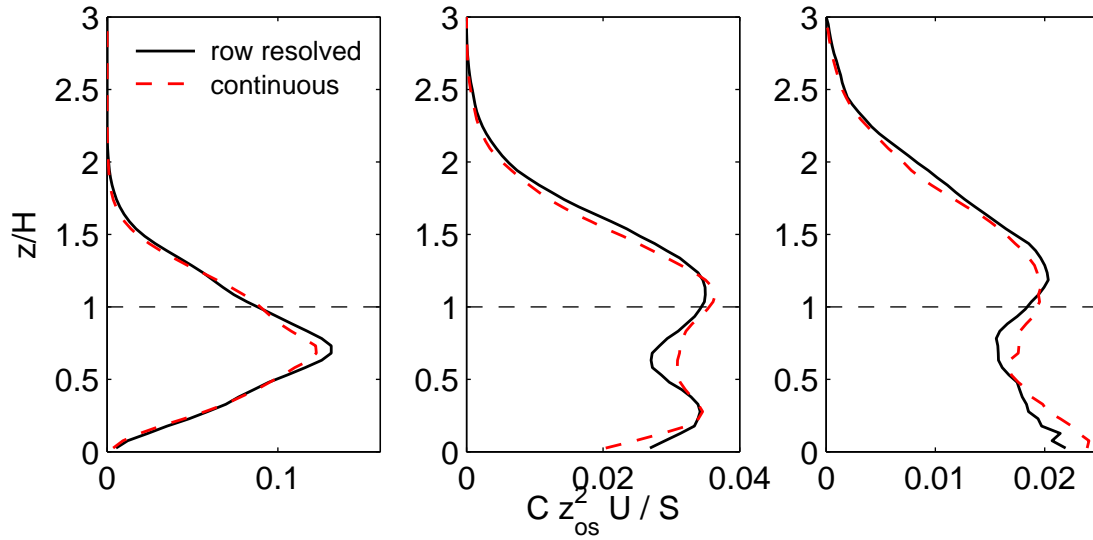
Figure 4.8. Particle concentration comparison for continuous and sparse representations of the vineyard.
Left Panel: X = 2.5 m. Middle Panel: X = 8.0 m. Right Panel: X = 15.0 m.
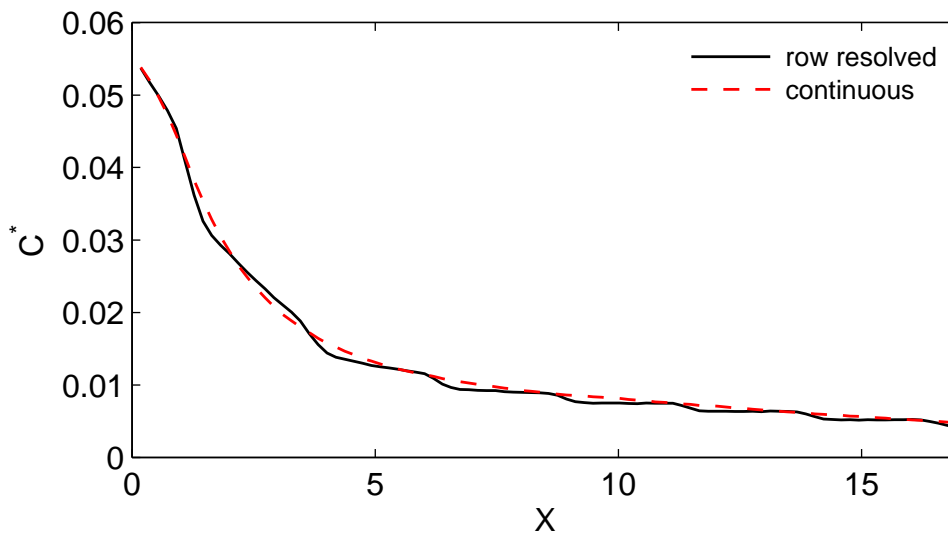
Figure 4.9. Particle concentration in the canopy as a function of downstream distance from the source. NOTE: $C^* = \frac{1}{H}\int_0^H C(z)dz$

vineyard canopy geometry has the potential to play an important role in the distance at which spores travel from their source. This section examines the effect of plant density and row spacing on the potential for disease spread. Near source concentration distributions were examined, as well as the potential for long-range particle transport.

Numerical experiments were conducted for LAI values of 1.0 and 3.0. This was determined to be a realistic range of values for actual grape vineyards, based on values reported by the Gladstone et al. 2003 data [20]. For each chosen value of LAI, a simulation was performed for row spacings of 1.0 m, 2.0 m, and 3.0 m, which represented a realistic cross-section, based on values reported by the Johnson et al.'s 2003 data [24]. The LAD profile shape was set according to measurements by the Gladstone et al. 2003 data [20] in which the LAD was measured at various heights for a vertical shoot positioned trellis/training system. This profile was then scaled to achieve the desired LAI. In each case, the flow was driven by an equivalent pressure gradient in the stream-wise direction, which had a value of 0.025 Pa/m. In this experiment, 100,000 particles were released over 5 minutes.

4.2.1   Velocity Statistics

Mean stream-wise velocity profiles are compared for six vineyard geometries in Fig. 4.10. Results indicate that as LAI is increased, the velocity in the area affected by the presence of the canopy tends to decrease as a result. This result makes sense intuitively, as higher plant density creates increased drag which should dissipate more momentum. A similar trend is observed as the row spacing is decreased. This is also to be expected because as the row spacing is decreased, there is a larger fraction of the domain occupied by vegetation. The apparent LAI is tabulated for each canopy geometry in Table 4.1, which was previously defined by eqn. 4.1. The apparent LAI is a measure of overall foliage density of the canopy. Thus, as the apparent LAI increases, the velocity in the canopy tends to decrease due to increased overall plant density. Figure 4.11 shows this trend of decreasing average stream-wise velocity in the canopy as a function of apparent LAI. When scaled by the friction velocity, u_*, the mean velocity decreases as an exponential function of apparent LAI (a plot of u_* is shown in Fig. 4.12.) The scaling relationship between U_c/u_* and $\overline{LAI}$ is
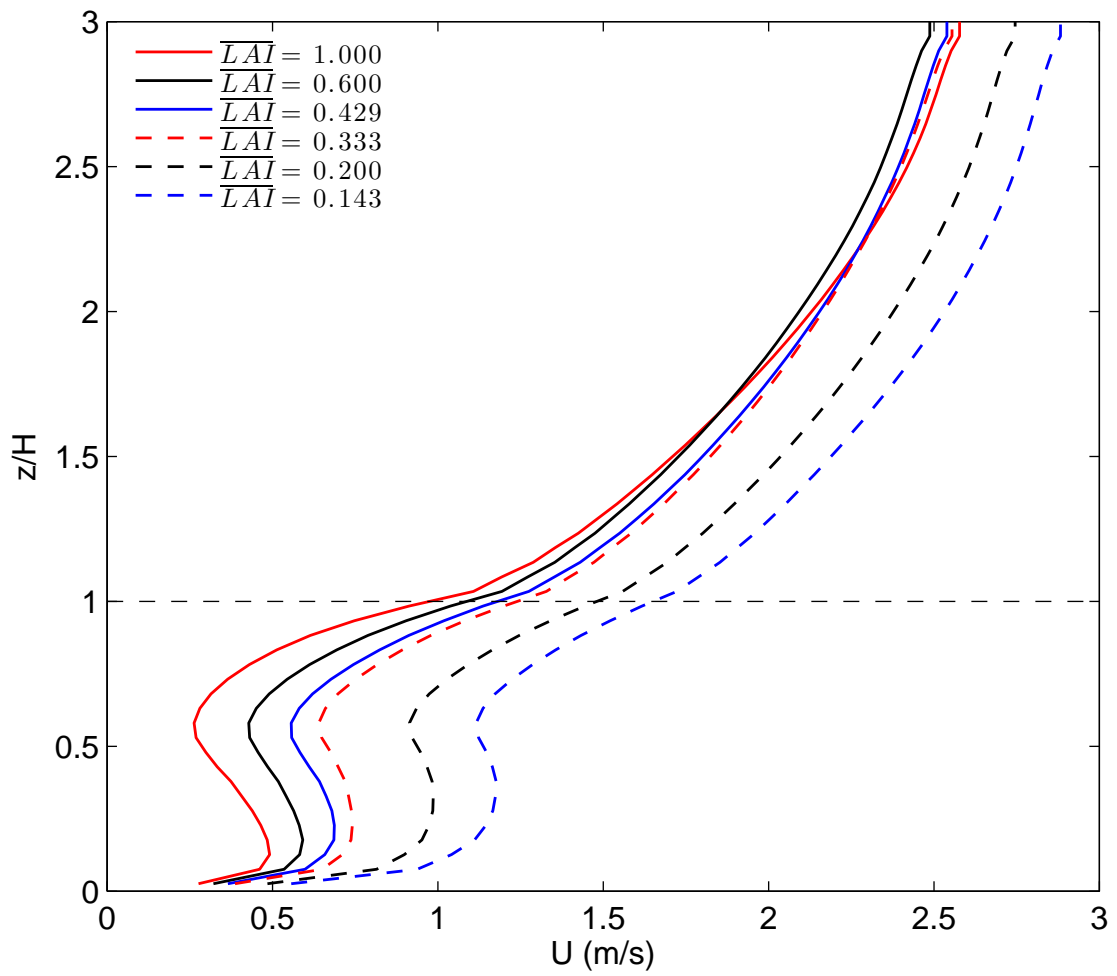
Figure 4.10. Comparison of mean stream-wise velocity profiles for six canopy geometries.

Table 4.1. Apparent LAI assuming a continuous canopy for vineyard geometries.

LAI	row spacing (m)	$\overline{LAI}$
3.0	1.0	1.000
3.0	2.0	0.600
3.0	3.0	0.429
1.0	1.0	0.333
1.0	2.0	0.200
1.0	3.0	0.143

$$U_c/u_* = \alpha \left(\overline{LAI}\right)^{-\beta}. \tag{4.3}$$

For this this group of simulations, $\alpha = 4.00$ and $\beta = 0.417$. The coefficient of determination, R^2, for the fit was 99.7%. This trend shows asymptotic behavior as the apparent LAI is increased. As the row spacing becomes smaller, the canopy begins to converge to a continuous canopy. This suggests that for small row spacing, the velocity becomes insensitive to changes in row spacing, and thus the sparse canopy begins to act as a continuous canopy.

The effect of foliage density on the vertical velocity variance at the top of the canopy was also examined, and is shown in Fig. 4.13. Results indicate that for a given LAI, the variance tended to decrease as the row spacing was decreased. However, when the variance is plotted as a function of apparent LAI, the trend seems to be discontinuous as row LAI is changed between 1.0 and 3.0. Although the vertical variance appears to follow a trend, values range from only about 0.33 to 0.36, which indicates that the variance could be effectively considered constant with change in apparent LAI. Stull [61] lists $\overline{\sigma_w^2}/u_*$ in the neutral surface layer as 2.5. The values at the canopy top obtained from the numerical experiments are significantly lower than those reported by Stull, as is expected considering the canopy top is not in the surface layer and the canopy tends to damp fluctuations. However, many researchers use correlations from the surface layer to approximate the variance near the canopy. This approach will likely lead to a significant overestimation of the variance.

This discontinuous trend is also seen when the canopy displacement height is examined. The canopy displacement height is the distance the logarithmic region is effectively shifted up as a result of the canopy. It can also be interpreted as the mean
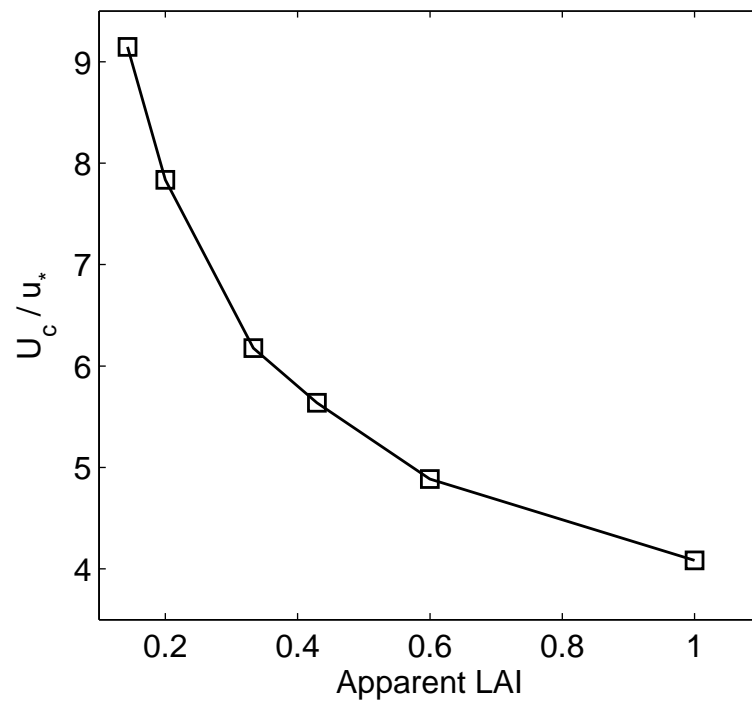
Figure 4.11. Comparison of canopy averaged stream-wise velocity for six canopy geometries. NOTE: $U_c = \frac{1}{H} \int_0^H U(z) dz$
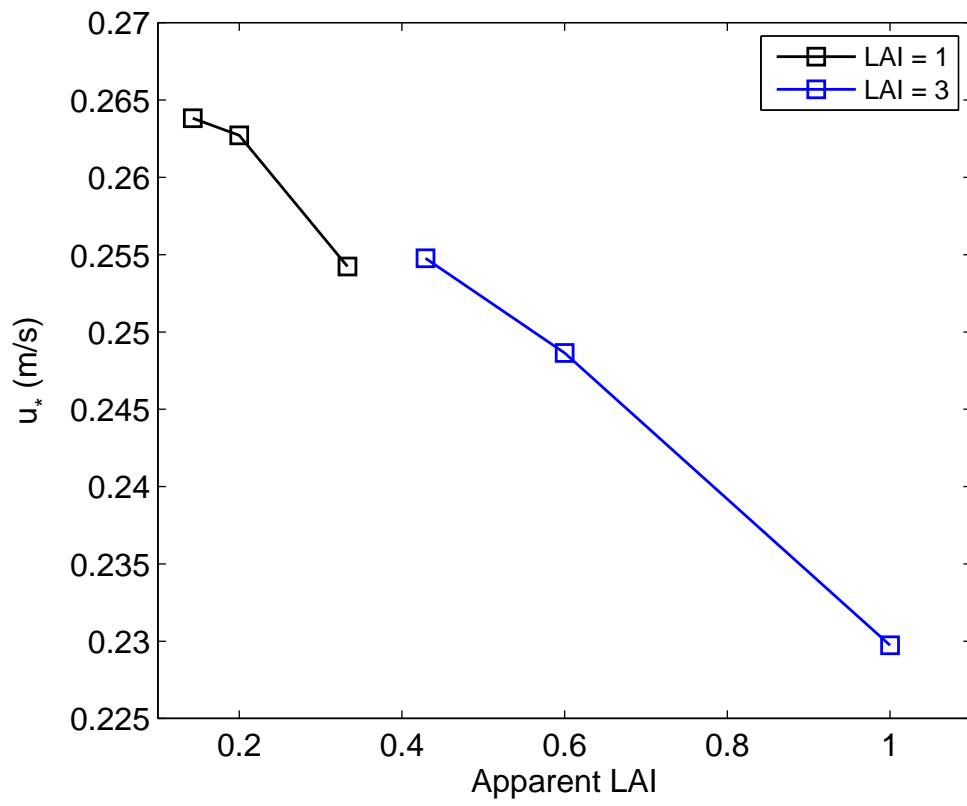
Figure 4.12. Comparison of the friction velocity, u_* for six canopy geometries.
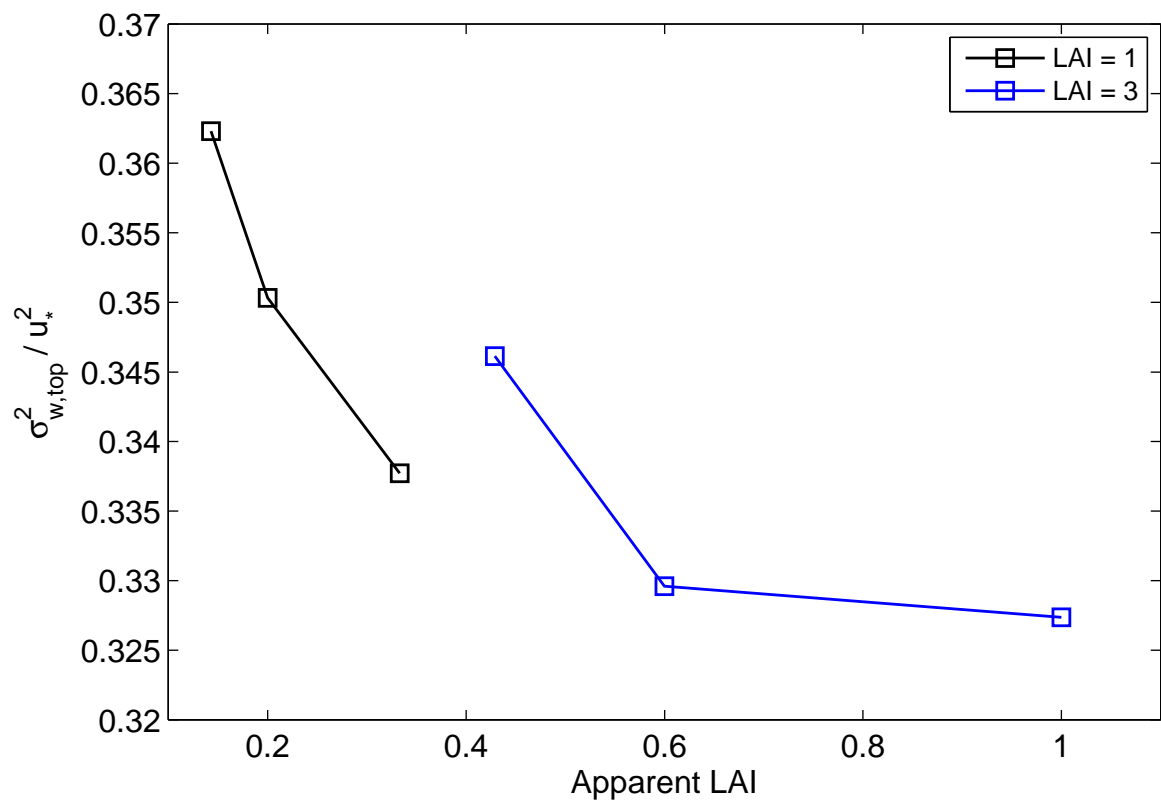
Figure 4.13. Comparison of vertical velocity variance at the top of the canopy for six canopy geometries.

amount of momentum absorption by the canopy [79]. With this interpretation, the displacement height can be estimated by integrating the momentum flux profile

$$d \approx h - \frac{1}{u_*} \int_0^h \langle u'w' \rangle \, \mathrm{d}z, \tag{4.4}$$

where h is the canopy height, u_* is the friction velocity at the canopy top, and $\langle u'w' \rangle$ is the horizontally averaged momentum flux. Figure 4.14 shows the displacement height plotted as a function of apparent LAI. For fixed LAI, the displacement height increases with increase in plant density. However, the displacement height is larger for $\overline{LAI}$=0.333 than $\overline{LAI}$=0.429, which opposes the general trend.

Although the trend is slightly discontinuous, an exponential function can be fit to the data to yield a correlation with reasonably high accuracy. The relationship between apparent LAI and displacement height was found to be

$$d/H = 0.945 \left(\overline{LAI} \right)^{0.0246}. \tag{4.5}$$

The coefficient of determination, R^2 for the fit was 98.2%, which indicates this correlation could be used with relatively high confidence for the range of apparent LAI presented in this numerical experiment, where error is likely dominated by modeling errors.

This discontinuous trend in both the vertical velocity variance and displacement height as functions of apparent LAI indicates that there are flow dynamics that are influencing these statistics besides overall plant density. One variable that is likely to play a significant role in this phenomenon is row spacing. The two cases at which the discontinuity in the trend occurs have very similar apparent LAI, but have different LAI and row spacing. It seems plausible that for similar apparent LAI, the case with a much smaller row spacing should have larger vertical variance and absorption of momentum. Smaller row spacing means that the flow will be impacting more rows, which will consequentially transfer more momentum to the vertical direction and also dissipate more momentum in the process.

Differences in turbulent structures between each vineyard case can dramatically influence the behavior of the velocity field. Figures 4.15 and 4.16 show fluctuation vectors $(\vec{V} = \langle u', w' \rangle)$ in the $x-z$ plane for each vineyard geometry. Plant density and
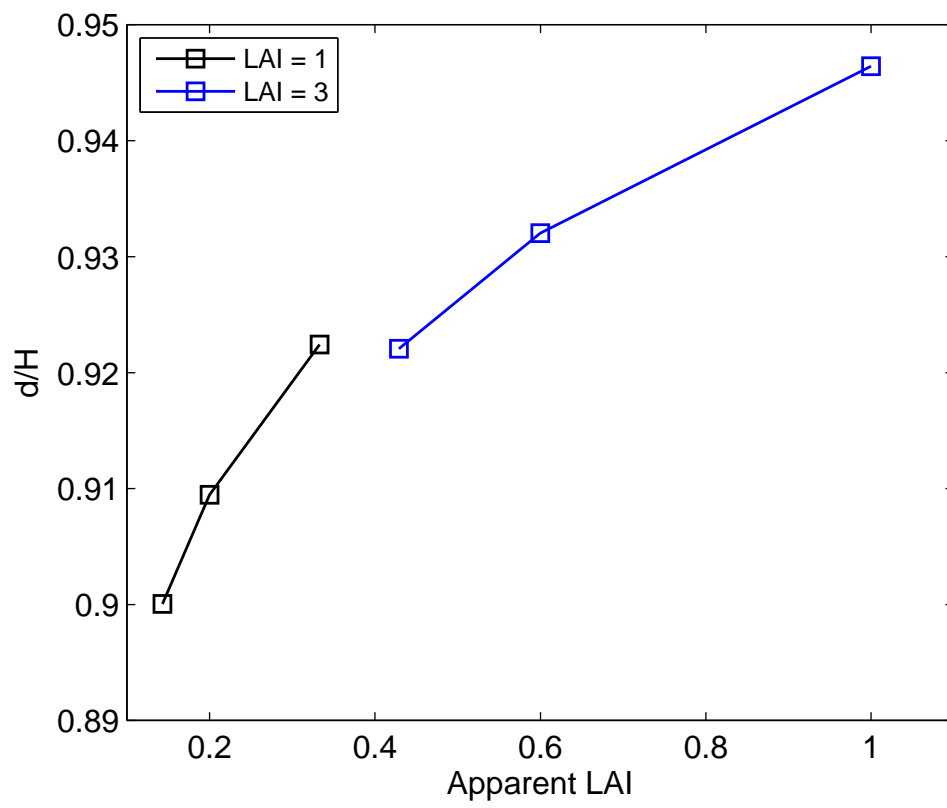
Figure 4.14. Comparison of canopy displacement height for six canopy geometries.

row spacing influence how coherent turbulence structures form in the spaces between rows. When row spacing is equal to 1.0 m, large vortices are not allowed to form because there is not enough space before the next row begins. Such motions tend to be damped out by the high row frequency.

Turbulent fluctuation vectors can be useful in visualizing the discontinuous trend observed in some of the previously presented statistics. Although the apparent LAI of the LAI = 1.0/spacing = 3.0 m and LAI = 3.0/spacing = 1.0 m are very similar, the turbulence structure is drastically different. In the case with the higher apparent LAI, turbulent fluctuations generally have low magnitude with a small characteristic length scale. Turbulent fluctuations are damped by the high row frequency. This explains the lower vertical variance in the higher apparent LAI case. Furthermore, the damping effect of high row frequency also seems to be one cause of the higher than expected displacement height.

4.2.2   Dispersion Statistics

To examine the effect of canopy geometry on near-source particle distributions, particle concentration was calculated at various downwind distances near the release point. The concentration profiles are compared in Fig. 4.17 for the six previously described vineyard geometries. Profiles are shown at three downstream distances. Concentrations are again normalized by the volume averaged stream-wise velocity to eliminate the dependence on stream-wise advection. If concentrations are not normalized, it is observed that increased velocity due to lower plant density tends to increase particle concentration. This is a somewhat trivial result and therefore results are shown normalized by the stream-wise velocity.

Results show little difference in concentrations immediately after release, with concentration profiles appearing to be approximately Gaussian. As particles move further downstream, concentrations generally tend to decrease in the canopy as apparent LAI is increased. One influence on this result is the fact that more vegetation elements result in a higher probability of deposition, thus reducing particle concentration.

Contrary to the previous statement, a similar discontinuous trend is observed as was found with the vertical velocity variance. There seems to be a jump in concentration as the row LAI is changed from 1.0 to 3.0. This is likely due to some
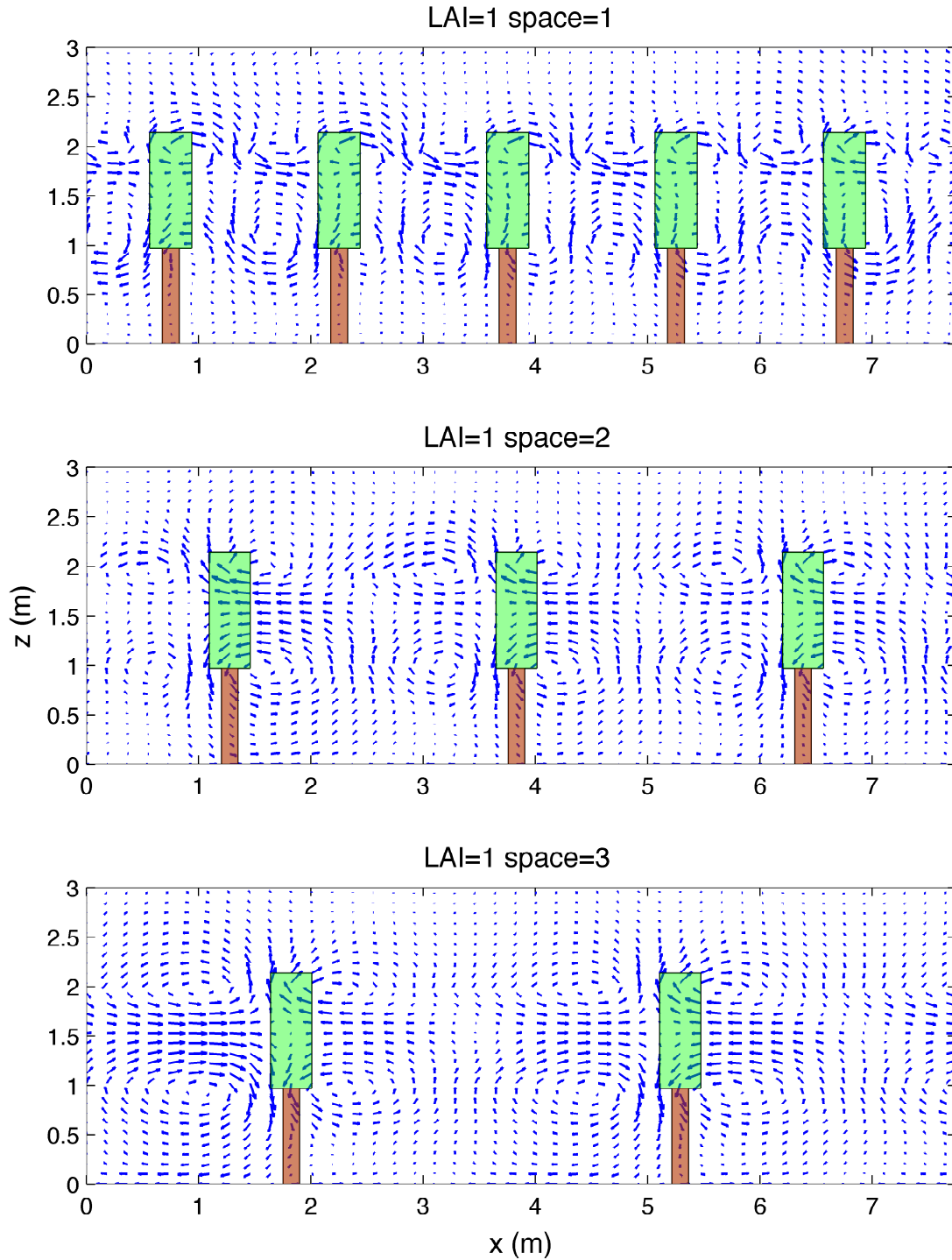
Figure 4.15. LAI $= 1$: Velocity fluctuation vectors ($\vec{V} = \langle u', w' \rangle$) in the x-z plane. Mean flow is from left to right.
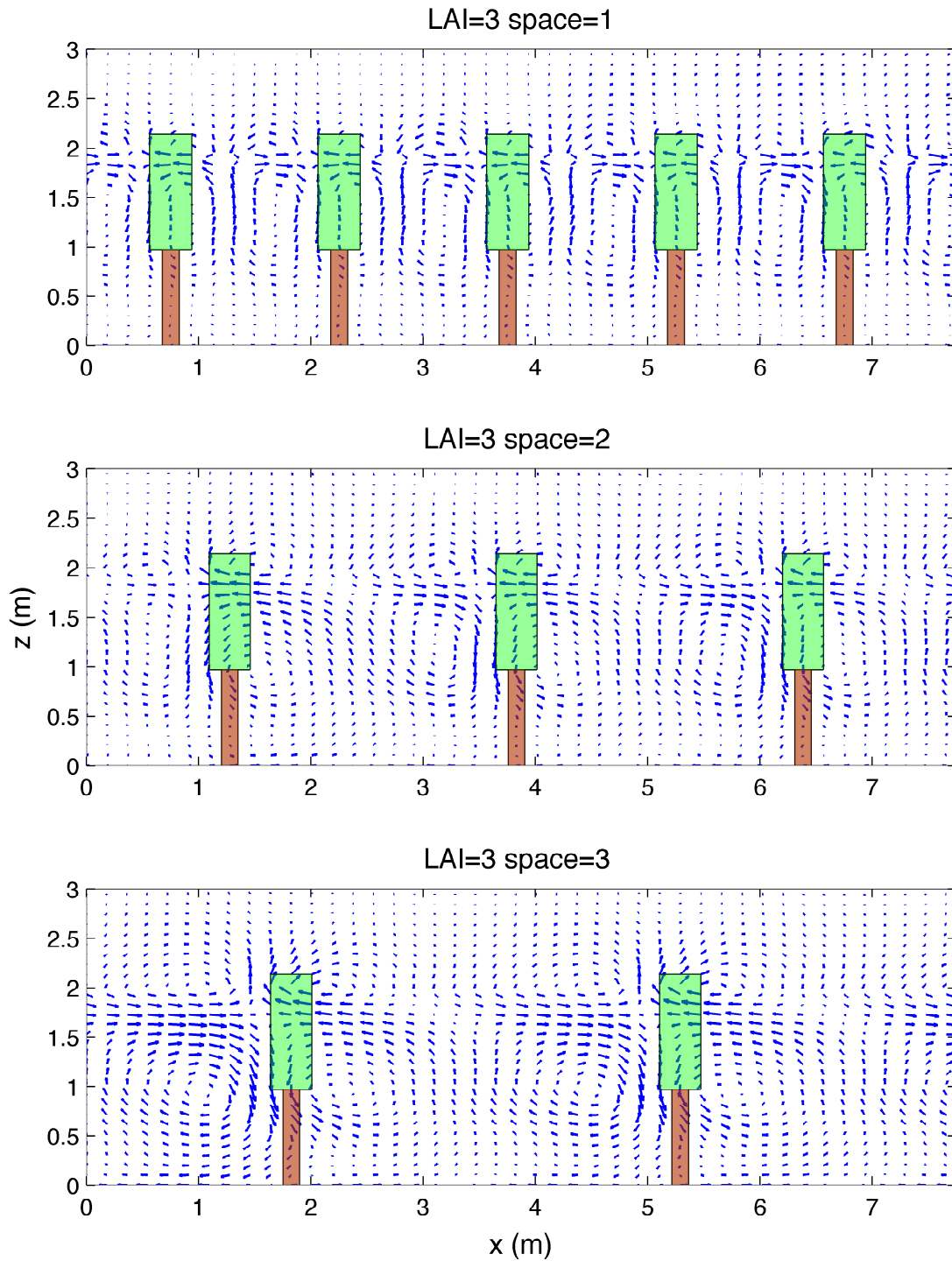
Figure 4.16. LAI $= 3$: Velocity fluctuation vectors ($\vec{V} = \langle u', w' \rangle$) in the x-z plane. Mean flow is from left to right.

Figure 4.17. Comparison of particle concentration profiles for six canopy geometries. Left Panel: X = 2.5 m. Middle Panel: X = 8.0 m. Right Panel: X = 15.0 m.

influence of the vertical velocity variance in the canopy, as well as the change in turbulence structure.

4.2.3 Potential for Long-Range Transport

Near source particle distributions are important in understanding the dynamics of particle transport and how plumes develop as they travel from the source. But ultimately the potential of rapid progression of epidemics is large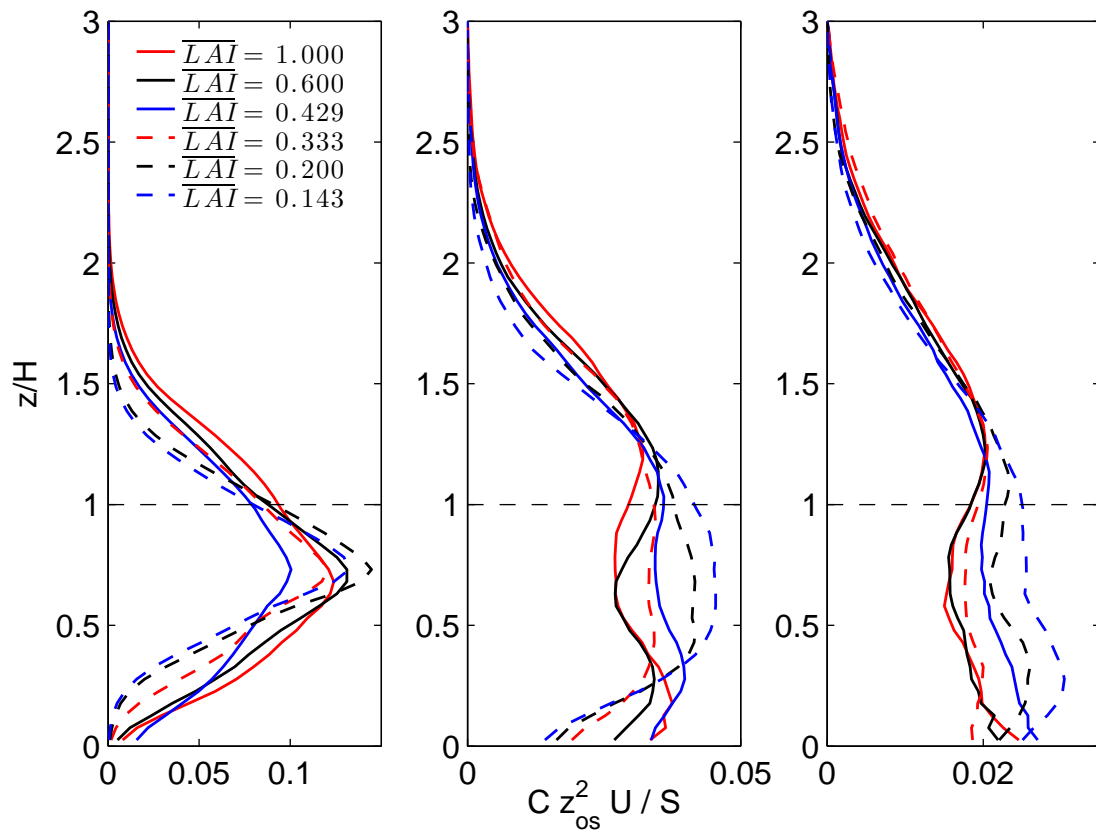ly determined by transport over large length scales. To examine how LAI and row spacing influence the potential for long-range transport, a numerical experiment was performed in which 100,000 particles were released from a line source and tracked for 5 minutes. After that time period, the absolute horizontal distance each particle had traveled from its source was recorded.

The probability density function (PDF) is shown in Fig. 4.18 for a single vineyard geometry. It is compared against a Gaussian distribution with the same mean and standard deviation. One noticeable difference between the two distributions is that the actual PDF is highly skewed. The Gaussian PDF is centered about its mean value, and extends infinitely in each direction (only a portion shown.) For the actual PDF, the most likely event is that a particle will be deposited in the first vegetation row. The figure also shows that there is a much higher probability for extreme events far away from the mean.

Table 4.2 shows a comparison of the mean and kurtosis of distance traveled from release point for each vineyard geometry. These results are also shown graphically in Fig. 4.19. Results show that increasing apparent LAI tended to decrease the average distance that particles traveled from the source. If the mean distance traveled is normalized by the average stream-wise velocity to form a "travel time," (also shown in Table 4.2,) particles generally tend to have the same travel time before becoming deposited on average as apparent LAI is varied. This demonstrates that advection is the dominating influence on the mean distance traveled by particles.

The kurtosis or flatness of distance traveled from source gives an indication of the probability of extreme events. A high kurtosis indicates that there is a high probability of particles traveling much further than the mean. From an epidemiology perspective, this means that there is a high probability of extreme transport
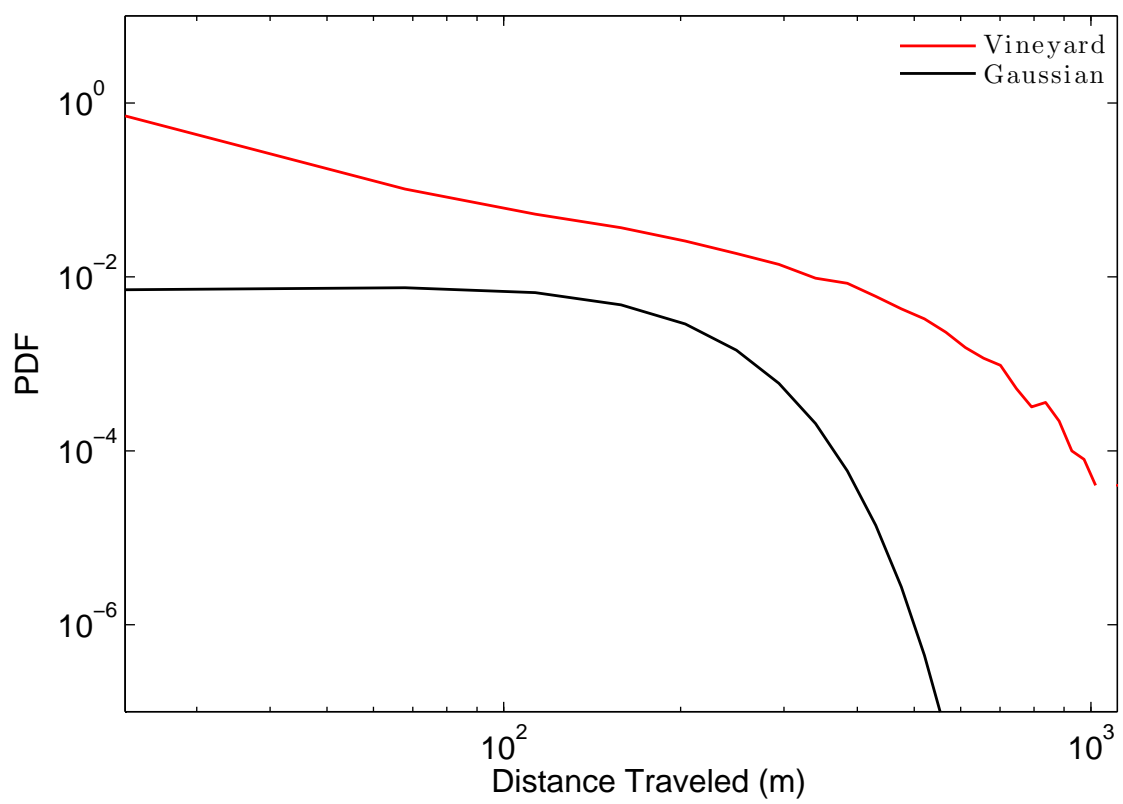
Figure 4.18. Probability density function of distance traveled by particles before becoming deposited compared with a standard Gaussian distribution (LAI = 3, spacing = 2 m.)
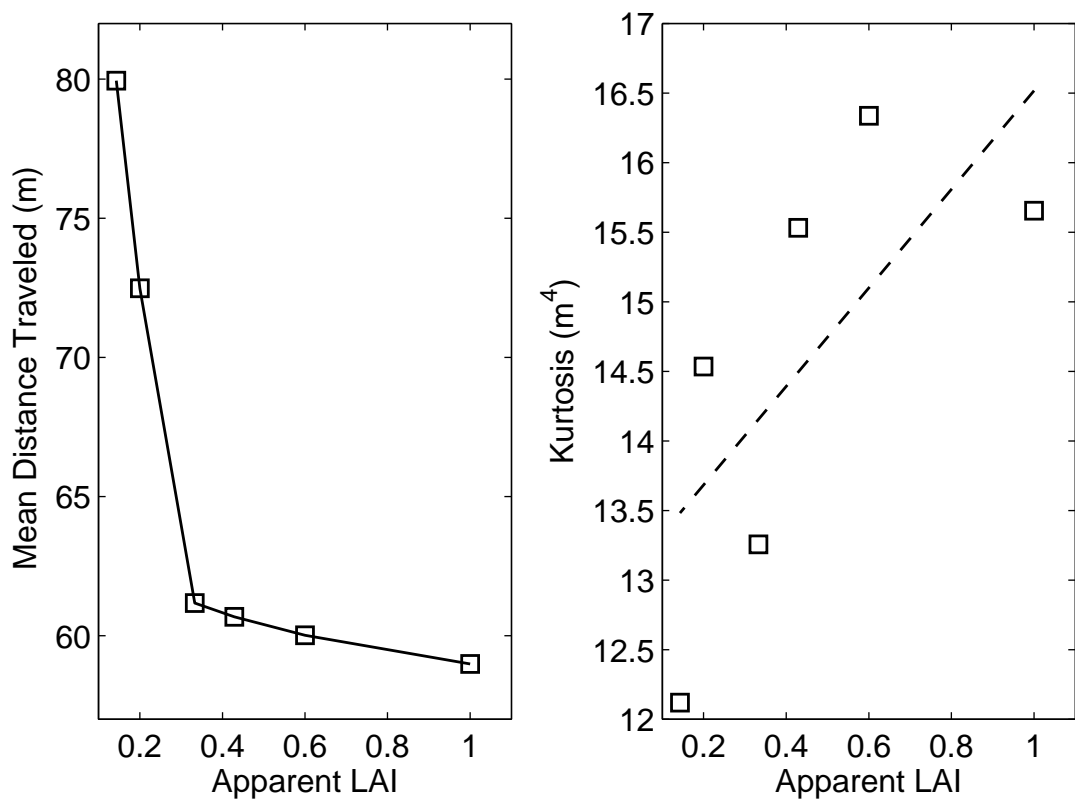
Figure 4.19. Mean and kurtosis of distance traveled from source.

**Table 4.2**. Long-range transport statistics.

$\overline{LAI}$	$\langle X \rangle$	$\langle X \rangle / U$	$\langle X^4 \rangle$
1.000	59.11	40.05	15.63
0.600	59.99	39.84	16.62
0.429	60.63	38.41	15.15
0.333	60.97	38.02	13.12
0.200	72.89	40.19	13.59
0.143	80.24	40.83	12.42

events, thus increasing the likelihood of infection on a large scale. Kurtosis values obtained from simulation results are not conclusive, but they indicate that, in general, increasing apparent LAI tends to increase kurtosis or extreme events.

As noted previously, another important influence on long range particle transport is canopy escape. Particles that escape the canopy are not directly influenced by the drag and deposition of the canopy. As a result, particles that are able to escape the canopy tend to travel further than particles that do not escape. Figure 4.20 shows the vertical flux of particles at the canopy top. Results show a generally increasing trend in canopy escape with increase in apparent LAI. Canopy escape also seems to be correlated with the kurtosis of distance traveled by particles. It seems reasonable that geometries with high canopy escape should yield high kurtosis in distance traveled from the source by particles.

4.2.3.1 Canopy Escape Neglecting Plant Deposition

The previous study of long-range particle transport revealed that increasing overall or "apparent" plant density in the vineyard tended to limit the probability of transport over large length scales. A significant influence on this behavior is deposition. More vegetation results in a higher probability of deposition, thus limiting transport. It is difficult to determine exactly what role deposition plays in the results and if there are other dynamics of the flow that also influence long-range transport. In an attempt to isolate the dynamics of the flow, a numerical experiment was performed to examine long-range transport as previously described, however plant deposition was ignored. Note that, although relatively insignificant, ground deposition was still included.
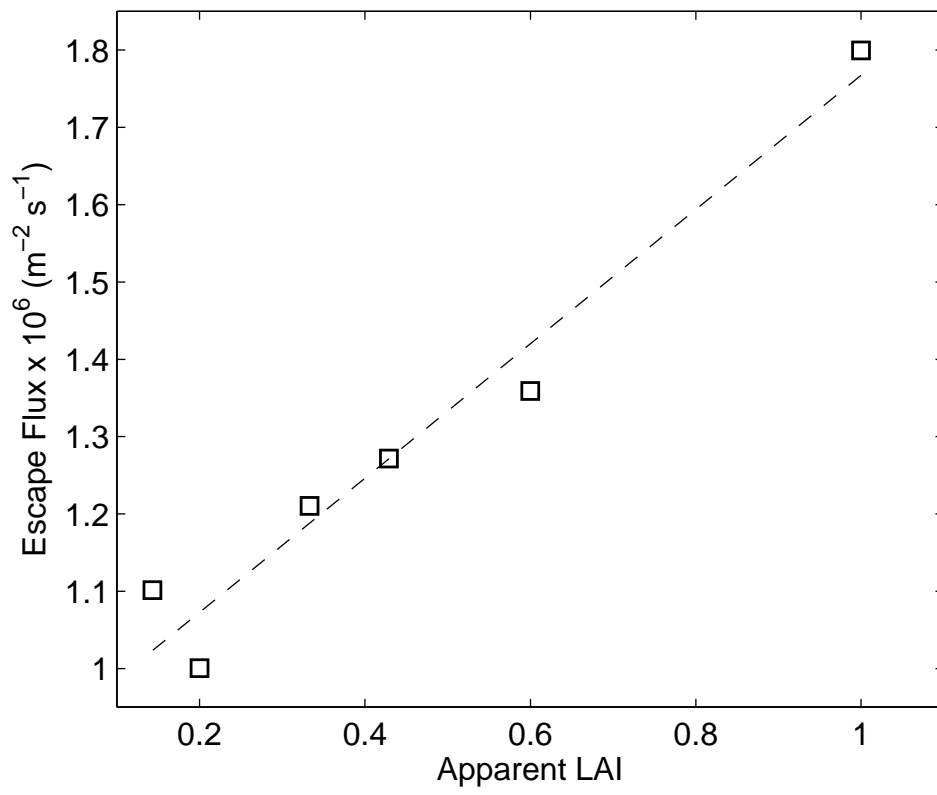
Figure 4.20. Vertical flux of particles at the canopy top.

Figure 4.21 shows the probability density function for a single simulation without deposition is compared against the same case with deposition and the Gaussian PDF. The PDF seems to follow the same trend as the Gaussian PDF. When compared to the case where deposition was included, deposition seems to cause a sharper drop in probability with larger distance traveled. There is larger area in the tails of the PDF when deposition is not considered, indicating that a larger amount of particles travel very long distances.

When the mean distance traveled by particles at the end of the simulation is examined, a similar trend is observed as when deposition was present (see Table 4.3 and Fig. 4.22.) As overall plant density is increased, particles seem to travel a shorter distance before the end of the simulation. Furthermore, the "travel times" for particles were also relatively constant, which is expected as particles generally travel for the same amount of time, as there is no plant deposition.

Although there is larger area in the tail of the PDF when deposition is not considered, the kurtosis is much smaller. This is due to the fact that the mean is much larger in the simulation with no deposition. The kurtosis is relatively constant when overall plant density is varied and has a value of about 3 m^4.

Table 4.3. Long-range transport statistics (no deposition.)

$\overline{LAI}$	$\langle X \rangle$	$\langle X \rangle / U$	$\langle X^4 \rangle$
1.000	231.20	153.24	3.37
0.600	244.58	159.10	3.27
0.429	251.29	155.52	3.16
0.333	265.56	160.90	2.89
0.200	303.84	162.37	2.91
0.143	322.77	159.06	2.90
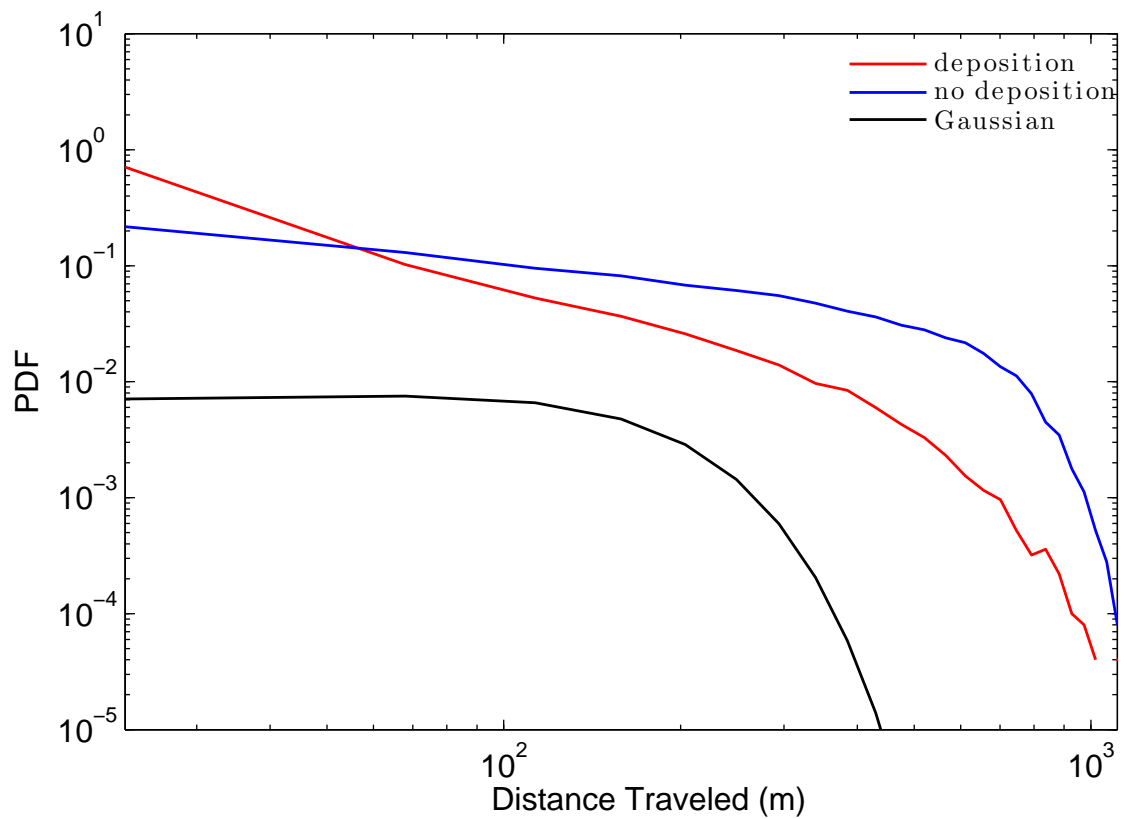
Figure 4.21. Probability density function of distance traveled by particles over a given time period neglecting deposition (LAI = 3, spacing = 2 m.) Plot is superimposed on Figure 4.18.
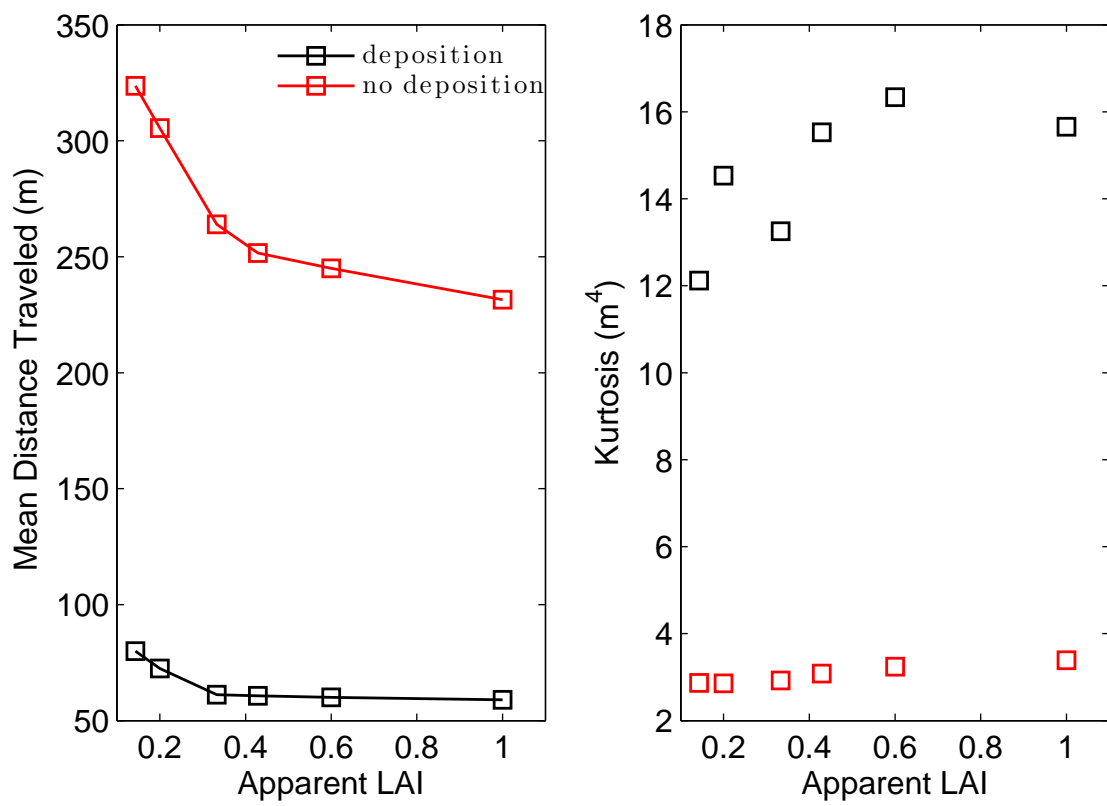
Figure 4.22. Mean and kurtosis of distance traveled from source without deposition. Plots are superimposed on figure 4.19.

CHAPTER 5

CONCLUSIONS

A series of large-eddy simulations were performed to analyze the dispersion of powdery mildew in grape vineyard canopies. A Lagrangian particle dispersion model was implemented that utilized Weil et al.'s adaptation of the Langevin equation to calculate the unresolved velocity component. A stochastic deposition model based on impaction of aerosols on circular cylinders was used to predict the probability of particle deposition on canopy foliage.

The models were validated against two experimental data sets: dispersion in a highly convective boundary layer [70] and dispersion in a continuous wheat canopy [4]. Models performed well when used to simulate the highly convective boundary layer case, which was largely due to the fact that the boundary layer was well resolved in the LES (i.e., $f_s \approx 20\%$.) The wheat canopy dispersion case was a more thorough model test, with f_s values ranging from about 50% to 75% in the canopy. The Lagrangian dispersion models explored in this thesis demonstrated insufficient mixing in the canopy. This could be due to insufficient turbulence levels in the LES solution or poor performance of the SFS particle velocity model. A conclusion cannot be made on the precise source of the lack of mixing based on the limited data set reported by Aylor and Ferrandino. However, as simulation results were examined further from the source (experimental values are reported at X = 4 m from the source) the models showed better mixing in the canopy.

In each simulation, 100,000 particles were released from a line source at 75% of the canopy height. The particles were allowed to travel until they were either deposited or the sampling time of 5 minutes was exceeded. The canopy was sufficiently resolved to model the discontinuous nature of the vineyard canopy. First, dispersion in a single vineyard geometry with a leaf area index of 3.0 and row spacing of 2.0 m was simulated to study the velocity field and dispersion characteristics of this type of flow.

Simulation results showed that, on average, the unresolved portion of the turbulent kinetic energy is greater than 50% in the canopy, thus emphasizing the importance of an adequate SFS velocity model for this type of flow. Furthermore, the discontinuous nature of the canopy seems to enhance vertical transport as the flow impacts each row.

To test the hypothesis that resolving the discontinuous canopy structure is important in obtaining accurate velocity and dispersion statistics, an "equivalent" continuous canopy was simulated that had the same apparent leaf area index as the previous vineyard case. The continuous representation of the canopy was able to predict the same mean velocity profile as the row-resolved representation. Results also showed that the continuous representation tended to yield slightly less particle escape from the canopy.

To examine the effect of canopy geometry on various velocity field and dispersion statistics, a series of six simulations were performed with leaf area index ranging from 1.0 to 3.0 and row spacing ranging from 1.0 m to 3.0 m. Results showed that as the overall density of the canopy was increased, the average velocity in the canopy decreased according to an exponential function. Other higher order velocity statistics did not follow a smooth trend with change in overall canopy density, and behaved according to a more complex function of LAI and row spacing. This result led to the investigation of turbulence structure in the canopy. The formation of coherent structures in the spaces between rows seemed to be dominated by row spacing, although plant density did play a role.

Simulations were also performed to examine how canopy geometry affected particle transport over large length scales. Results showed that particles tended to travel further, on average, when overall canopy density was decreased. This was shown to be dominated by mean stream-wise advection. Decreasing overall canopy density also tended to decrease the probability of particles traveling much further than the mean. This decrease seemed to correspond with the decrease in canopy escape.

Nearly all statistics tended to converge to an asymptotic value as overall canopy density became large. Thus, as canopy density becomes sufficiently large, the canopy begins to act as a continuous, dense canopy. At this point, it seems acceptable

to represent the canopy as continuous and not resolve row structure. However, for realistic values of vineyards that are normally observed, this approximation will likely introduce significant inaccuracies in results.

5.1   Future Work

5.1.1   Domain Size and the Top Boundary Condition

For the preceding results, the assumption was made that the chosen domain height was large enough to allow all important coherent turbulence structures to form. Furthermore, it was also assumed that there was no stress at the top of the boundary, implicitly implying that the domain height is at or above the boundary layer height. The overwhelming majority of researchers choose a domain height near three canopy heights (e.g., [4, 54, 79, 17]), with little or no discussion of the implications of such a choice. Truncating the domain height could neglect the effects of large eddies that may be important to long-distance transport. Furthermore, assuming zero stress at the top of the domain could dramatically alter the velocity field in and above the canopy.

A simulation was run that was identical to the LAI = 3.0/row spacing = 2.0 m case, however the dimensions of the domain were increased to $2L_x \times L_y \times 2L_z$. Figure 5.1 shows a comparison of the velocity profiles for the "small" and "large" domain sizes. This figure shows that assuming zero stress at the top of the domain when the domain height is below the boundary layer height effectively decreases the velocity above the canopy. It appears that the velocity in the bottom half of the canopy is relatively unaffected by the domain size. This result is likely dominated by the top boundary condition. If the domain height is below the top of the boundary layer, in general there will be some stress at the top boundary, and as a result the velocity profile will not flatten out to zero slope.

Figure 5.2 shows concentration profiles for both domain size choices. Results show that increasing the domain size tends to increase particle concentrations inside the canopy. The differences become larger as particles move further downstream from the source.

The obvious solution to this problem is to increase the domain height to the top of the boundary layer. To keep the same resolution in the canopy, this would result
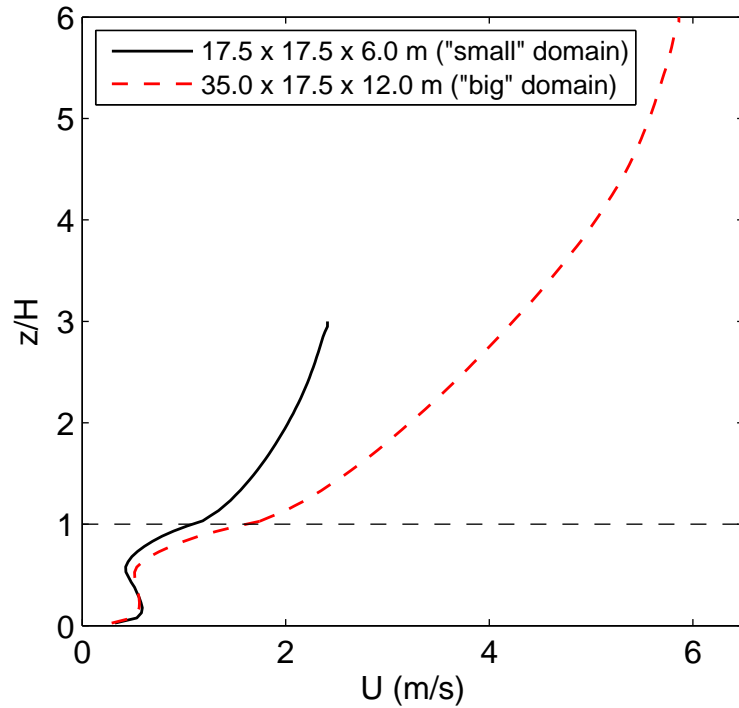
Figure 5.1. Comparison of the stream-wise velocity for the "small" and "large" domain sizes.
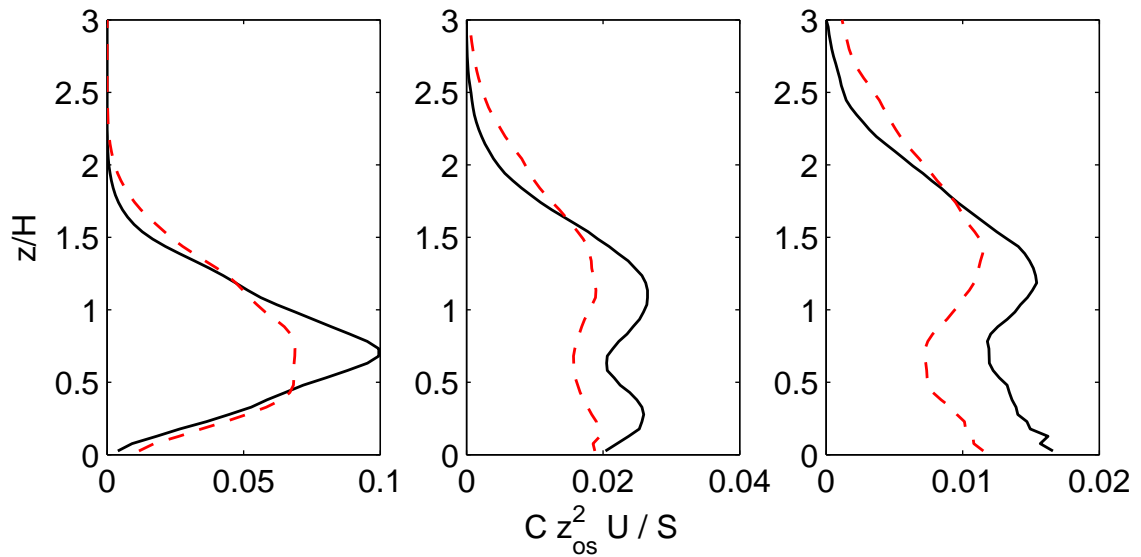
Figure 5.2. Comparison of particle concentration for the "small" and "large" domain sizes.
Left Panel: X = 2.5 m. Middle Panel: X = 8.0 m. Right Panel: X = 15.0 m. For legend, see fig. 5.1.

in and extremely large number of computational nodes, as the horizontal domain size must also be increased to obtain an acceptable grid aspect ratio. One possible method to improve results without increasing domain height would be to use the log-law to estimate the stress at the top of the boundary. If the displacement height is known, a logarithmic profile can be used to estimate the slope at the top boundary. However, a similar problem arises as when the bottom boundary condition is specified. Although on average the stress is zero in the span-wise direction, the stress may not be zero instantaneously. As a result the stress in the span-wise direction is specified by vector decomposition of the log-law. This would likely produce similar errors as are present at the bottom boundary, but may significantly improve results overall.

Another solution is to use a domain height above the boundary layer height and use a refined grid in the area near the canopy. This would allow for the desired resolution in the canopy and coarser resolution above the canopy, while still keeping the same number of computational nodes. This would also require grid refinement in the horizontal directions in order to preserve the grid aspect ratio. Grid refinement in the horizontal directions can be problematic when using pseudospectral methods.

5.1.2   Further Validation

Although the previously presented models have been validated for a continuous canopy, a comparison to empirical data for a sparse canopy, specifically a vineyard, has yet to be performed. To further validate the models, numerical results will be compared to field data for an experimental vineyard. Some field experiments have been performed that produced questionable data. It is not clear at this time how reliable the results from previous experiments are. However, a second iteration of the field experiment is planned. Future data along with past data should provide a reliable data set with which the numerical models may be compared.

If future experimental results indicate that current dispersion models may be inadequate, specifically in sparse canopy geometries, work may be done to formulate models which are general enough to be applied to such heterogeneous and anisotropic flows such as the vineyard.

APPENDIX

SIMULATION INPUTS

A.1   Willis and Deardorff Validation Case

Table A.1. LES inputs for the Willis and Deardorff validation case.
$N_x \times N_y \times N_z$ is the number of grid points, $L_x \times L_y \times L_z$ is the domain size, $\overline{w\theta_o}$ is the surface heat flux, z_o is the surface aerodynamic roughness height, $U - g$ is the geostrophic wind, Θ_0 is a buoyancy reference temperature, and f_c is the Coriolis parameter.

$N_x \times N_y \times N_z$	$L_x \times L_y \times L_z$ (km)	$\overline{w\theta_o}$ (m-K/s)	$z_{i,o}$ (m)	z_o (m)	U_g (m/s)	Θ_0 (K)	f_c
96^3	$5 \times 5 \times 2$	0.24	850	0.16	3.6	294	1.5

Table A.2. Particle model inputs for the Willis and Deardorff case.
N is number of particles, Δt_p is the timestep for updating particle positions, z_r is the release height, and C_0 is a SFS model parameter.

N	Δt_p (s)	z_r (m)	C_0
72,900	1.0	70	3.0

A.2   Aylor and Ferrandino Validation Case

Table A.3. LES inputs for the Aylor and Ferrandino validation case.
$N_x \times N_y \times N_z$ is the number of grid points, $L_x \times L_y \times L_z$ is the domain size, $\partial p/\partial x$ is the forcing pressure gradient, z_o is the surface aerodynamic roughness height, and H is the canopy height.

$N_x \times N_y \times N_z$	$L_x \times L_y \times L_z$ (m)	U (m/s)	z_o (m)	H (m)
$96 \times 96 \times 60$	$17.9 \times 17.9 \times 2.85$	1.84	0.01	0.95

Table A.4. Particle model inputs for the Aylor and Ferrandino validation case.
N is number of particles, Δt_p is the timestep for updating particle positions, z_r is the release height, C_0 is a SFS model parameter, L_v is the characteristic size of vegetation elements, f_x and f_z are the fractions of plant area projected onto horizontal and vertical planes, v_s is the particle settling velocity.

N	Δt_p (s)	z_r (m)	C_0	L_v (m)	f_x	f_z	v_s (m)
30,000	0.059	0.76	3.0	0.004	0.5	0.1	0.0194

A.3 Vineyard Cases

Table A.5. LES inputs for the vineyard case.
$N_x \times N_y \times N_z$ is the number of grid points, $L_x \times L_y \times L_z$ is the domain size, $\partial p/\partial x$ is the forcing pressure gradient, z_o is the surface aerodynamic roughness height, H is the canopy height, and w is row width.

$N_x \times N_y \times N_z$	$L_x \times L_y \times L_z$ (m)	$\partial p/\partial x$ (Pa/m)	z_o (m)	H (m)	w (m)
$96 \times 96 \times 60$	$17.5 \times 17.5 \times 2.0$	0.025	0.01	2.0	0.5

Table A.6. Particle model inputs for the vineyard case.
N is number of particles, Δt_p is the timestep for updating particle positions, z_r is the release height, C_0 is a SFS model parameter, L_v is the characteristic size of vegetation elements, f_x and f_z are the fractions of plant area projected onto horizontal and vertical planes, v_s is the particle settling velocity.

N	Δt_p (s)	z_r (m)	C_0	L_v (m)	f_x	f_z	v_s (m)
100,000	0.06	1.75	3.0	0.005	0.5	0.5	0.02
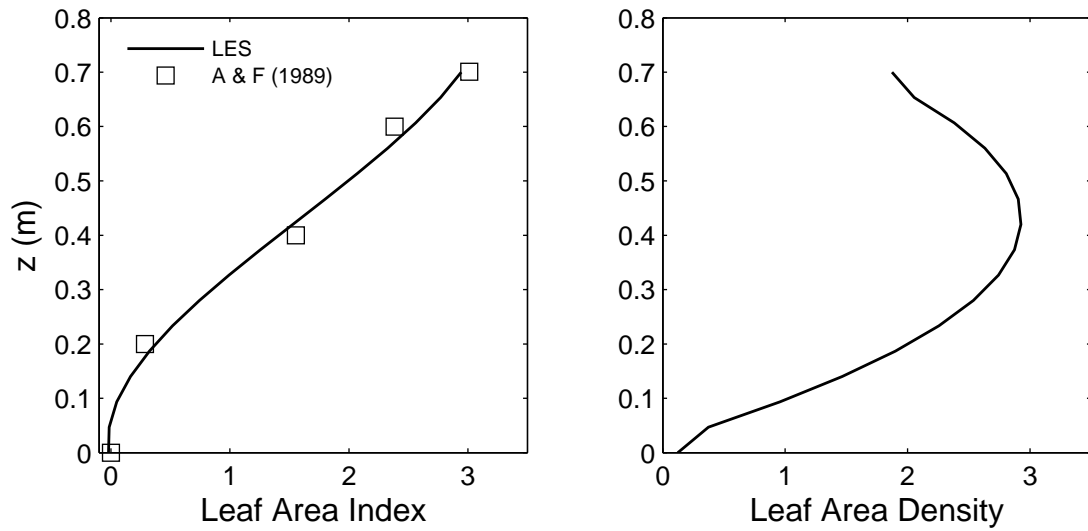
Figure A.1. Leaf Area Index and Leaf Area Profiles for the Aylor and Ferrandino validation case.
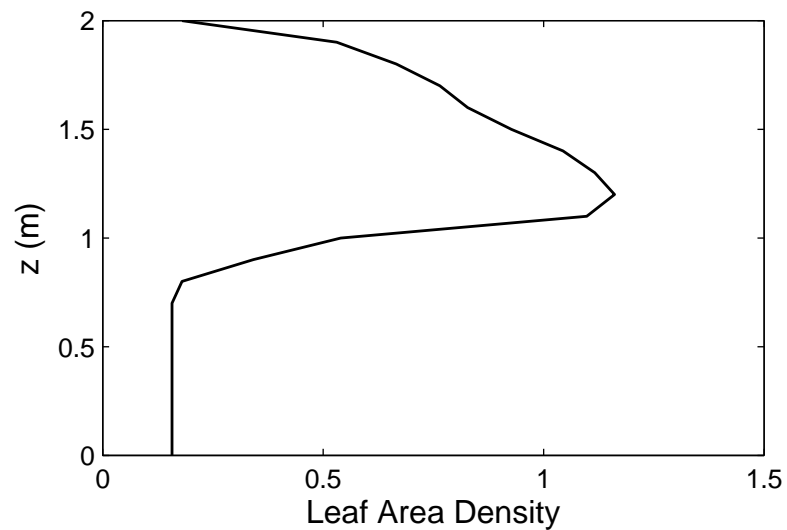
Figure A.2. Leaf Area Index and Leaf Area Profiles for the vineyard cases.

REFERENCES

[1] AGRIOS, G. N. *Plant Pathology;* Elsevier Academic Press: New York, 2006.

[2] AYLOR, D. E. Modeling spore dispersal in a barley crop. *Agr. Meteorol.* **1982**, 26, 215–219.

[3] AYLOR, D. E.; TAYLOR, G. S. Escape of peronospora tabacina spores from a field of diseased tobacco plants. *Pytopathology* **1983**, 73, 525–529.

[4] AYLOR, D. E.; FERRANDINO, F. J. Dispersion of spores released from a elevated line source within a wheat canopy. *Bound.-Lay. Meteorol.* **1989**, 46, 251–273.

[5] AYLOR, D. E. Biophysical scaling and the passive dispersion of fungus spores: relationship to integrated pest management stratagies. *Agr. Forest Meteorol.* **1999**, 97, 275–292.

[6] BARDINA, J.; FERZIGER, J. H.; REYNOLDS, W. C. *Improved subgrid models for large eddy simulation.* Paper 80-1357, AIAA, 1980.

[7] BORGAS, M. S.; SAWFORD, B. L. A family of stochastic models for two-particle dispersion in isotropic homogeneous stationary turbulence. *J. Fluid Mech.* **1994**, 279, 69–99.

[8] BORGAS, M. S.; YEUNG, P. K. A Conditional fluid-particle accelerations in turbulence. *Theo. Comp. Fluid Dynam.* **1998**, 11, 69–93.

[9] BOHRER, G.; KATUL, G. G.; NATHAN, R.; WALKO, R. L.; AVISSAR, R. Effects of canopy heterogeneity, seed abscission and inertia on wind-driven dispersal kernels of tree seeds. *J. Ecol.* **2008**, 96, 569–580.

[10] CAI, X.; ZHANG, R.; LI, Y. A large-eddy simulation and lagrangian stochastic study of heavy particle dispersion in the convective boundary layer. *Bound.-Lay. Meteorol.* **2006**, 120, 413–435.

[11] CHAMECKI, M.; MENEVEAU, C.; PARLANGE, M. B. Large eddy simulation of pollen transport in the atmospheric boundary layer. *Aerosol Sci. Tech.* **2009**, 40, 241–255.

[12] DAVIES, C. N. Deposition from moving aerosols. In *Aerosol Science;* C.N. Davies, Ed.; Academic Press: New York, 1974; pp 393–446.

[13] DEARDORFF, J. W. Three-dimensional numerical study of the height and mean structure of a heated planetary boundary layer. *Bound.-Lay. Meteorol.* **1974**, 18, 81–106.

[14] FERZIGER, J. H; AND PERIČ, M. *Computational Methods for Fluid Dynamics;* Springer-Verlag: New York, 2002.

[15] FINNIGAN, J. J. *Turbulent Transport in Flexible Plant Canopies;* B. A. Hutchison and B. B. Hicks, Eds; D. Reidel Publishing Company: Dordrecht/Boston/Lancaster, 1985; pp 443–480.

[16] FINNIGAN, J. J. Turbulence in plant canopies. *Ann. Rev. Fluid Mech.* **2000**, 32, 519–571.

[17] FINNIGAN, J. J.; SHAW, R. H.; AND PATTON, E. G. Turbulence structures above a vegetation canopy. *J. Fluid Mech.* **2009**, 637, 387-424.

[18] FLESCH, T. K.; WILSON, J. D. A two-dimensional trajectory-simulation model for non-Gaussian, inhomogeneous turbulence within plant canopies. *Bound.-Lay. Meteor.* **1992**, 61, 349–374.

[19] GERMANO, M.; PIOMELLI, U.; MOIN, P.; CABOT, W. H. A dynamic subgrid-scale eddy viscosity model. *Phys. Fluids A* **1991**, 3, 1760–1765.

[20] GLADSTONE, E. A.; DOKOOZLIAN, N. K. Influence of leaf area density and trellis/training system on the light microclimate within grapevine canopies. *Vitis* **2003**, 42, 123–131.

[21] GOPALAKRISHNAN, S. G., AVISSAR, R. An LES study of the impacts of land surface heterogeneity on dispersion in the convective boundary layer. *J. Atmos. Sci.* **1990**, 57, 352–371.

[22] HEPPE, B. M. O. Generalized Langevin equation for relative turbulent dispersion. *J. Fluid Mech.* **1998**,357, 167–198.

[23] JANICKE, L. Particle simulation of inhomogeneous turbulent diffusion. In *Air Pollution Modelling and Its Application II*; Plenum 1983; pp 527–535.

[24] JOHNSON, L. F.; ROCZEN, D. E.; YOUKHANA, S. K.; NEMANI, R. R.; BOSCH, D. F. Mapping vineyard leaf area with multispectral satellite imagery. *Comput. Elect. Agri.* **2003**, 38, 33–44.

[25] KIM, S. W., MOENG, C. H., WEIL, J. C., BARTH, M. C. Lagrangian particle dispersion modeling of the fumigation process using large-eddy simulation. *J. Atmos. Sci.* **2005**, 62, 1932–1946.

[26] JONES, W. P.; LAUNDER, B. E. The prediction of laminarization with a two-equation model of turbulence. *Internat. J. Heat Mass Transf.* **1972**, 15, 301–314.

[27] LEWELLEN, W. S., TESKE, M. Prediciton of the Monin-Obukhov similarity functions from an invariant model of turbulence. *J. Atmos. Sci.* **1973**, 30, 1340–1345.

[28] LEGG, B. J.; POWELL, F. A. Spore dispersal in a barley crop: a mathematical model. *Agr. Meteorol.* **1979**, 20, 47–67.

[29] LI, Z.; LIN, J. D.; MILLER, D. R. Air flow over and through a forest edge: a steady-state numerical simulation. *Bound.-Lay. Meteorol.* **1990**, 51, 179–197.

[30] LILLY, D. K. The representation of small-scale turbulence in numerical simulation experiments. In *Proc. IBM Scientific Computing Symp. on Environmental Sciences*; H. H. Goldstine (Ed.); Yorktown Heights, NY, 1967; pp 195–210.

[31] LUHAR, A. K.; BRITTER, R. E. A random walk model for dispersion in inhomogeneous turbulence in a convective boundary layer. *Atmos. Env.* **1989**, 23, 1911–1924.

[32] MASON, P. J.; CALLEN, N. S. On the magnitude of the subgrid-scale eddy coefficient in large-eddy simulations of turbulent channel flow. *J. Fluid Mech.* **1986**, 162, 439–462.

[33] MAY, K. R.; CLIFFORD, R. The impaction of aerosol particles on cylinders, spheres, ribbons and discs. *Ann. Occ. Hyg.* **1967**, 10, 83–95.

[34] McCARTNEY, H. A.; FITT, B. D. L.; WEST, J. S. *The Epidemiology of Plant Diseases.* D. G. Jones and B. Kaye, Eds.; Springer: New York, 2006; pp 159–192.

[35] MELLOR, G. L.; YAMADA, T. Development of a turbulence closure model for geophysical fluid problems. *Rev. Geophys. and Space Phys.* **1982**, 20, 851–875.

[36] MENEVEAU, C.; KATZ, J. Scale-invariance and turbulence models for large-eddy simulation. Ann. Rev. Fluid Mech. **2000**, 32, 1–32.

[37] MOENG, C. H. A large-eddy simulation model for the study of planetary boundar layer turbulence. *J. of Atm. Sci.* **1984**, 41, 2052–2062.

[38] MOENG, C. H.; SULLIVAN, P. P. A comparison of shear- and buoyancy- driven planetary boundary layers. *J. of Atm. Sci.* **1994**, 51, 1–26.

[39] MOIN, P.; KIM, J. Numerical investigation of turbulent channel flow. *J. Fluid Mech.* **1982**, 219, 341–377.

[40] MONIN, A. S.; YAGLOM, A. M. *Statistical Fluid Mechanics,* Vol. 2; M.I.T. Press: Boston, MA; 1975.

[41] PASQUILL, F.; SMITH, F. B. *Atmospheric Diffusion;* John Wiley and Sons: New York; 1983.

[42] PATTON, E. G.; SHAW, R. H.; JUDD, M. J.; RAUPACH, M. R. Large-eddy simulation of windbreak flow. *Bound.-Lay. Meteorol.* **1998**, 87, 275–307.

[43] PIOMELLI, U. High Reynolds number calculations using the dynamic subgrid-scale stress model. *Phys. of Fluids A* **1993**, 5, 1484–1490.

[44] POPE, S. B. *Turbulent Flows*; Cambridge University Press: Cambridge; 2001.

[45] PORTÈ-AGEL F.; MENEVEAU, C.; PARLANGE, M. B. A scale-dependent dynamic model for large-eddy simulations: application to a neutral atmospheric boundary layer. *J. Fluid Mech.* **2000**, 415, 261–282.

[46] PORTÈ-AGEL, F.; PAHLOW, M.; MENEVEAU, C.; PARLANGE, M. B. Atmospheric stability effect on subgrid-scale physics for large-eddy simulation. *Adv. in Water Resour.* **2001**, 24, 1085–1102.

[47] RAUPACH, M. R.; THOM, A. S. Turbulence in and above plant canopies. *Ann. Rev. Fluid Mech.* **1981**, 13, 97–129.

[48] RAUPACH, M. R.; COPPIN, P. A.; LEGG, B. J. Experiments on scalar dispersion within a model plant canopy. Part I: the turbulence structure. *Bound.-Lay. Meteorol.* **1986**, 22, 79–90.

[49] RAUPACH, M. R.; FINNIGAN, J. J.; BRUNET, Y. Coherent eddies and turbulence in vegetation canopies: the mixing-layer analogy. *Bound.-Lay. Meteorol.* **1996**, 78, 351–382.

[50] RUIJGROK, W.; TIEBEN, H.; EISINGA, P. The dry deposition of particles to a forest canopy: A comparison of model and experimental results. *Atmos. Env.* **1997**, 31, 399–415.

[51] SAWFORD, B. L. Reynolds number effects in Lagrangian stochastic models of turbulent dispersion. *Chem. Eng. Sci.* **1986**, 44, 81–99.

[52] SHAMSUDDIN, I.; DOUGLAS, P. L. Inertial impaction of aerosol particles on cylinders at intermediate and high reynolds numbers. *Chem. Eng. Sci.* **1986**, 44, 81–99.

[53] SHAW, R. H.; SILVERSIDES, R. H.; THURTELL, G. W. Some observations of turbulence and turbulent transport within plant canopies. *Bound.-Lay. Meteorol.* **1974**, 5, 429–449.

[54] SHAW, R. H.; SCHUMANN, U. Large-eddy simulation of turbulent flow above and within a forest. *Agr. Forest Meteorol.* **2003**, 115, 5–17.

[55] SHAW, R. H.; PATTON, E. G. Canopy element influences on resolved- and subgrid-scale energy within a large-eddy simulation. *Bound.-Lay. Meteorol.* **1992**, 61, 47–64.

[56] SLINN, W. G. N. Predictions for particle deposition to vegetative canopies. *Atmos. Env.* **1982**, 16, 1765–1794.

[57] SMAGORINSKY, J. General circulation experiments with the primitive equations, part1: The basic experiment. *Month. Weather Rev.* **1963**, 91, 99–164.

[58] SORBJAN, Z.; ULIASZ, M. Large-eddy simulation of air pollution dispersion in the nocturnal cloud-topped atmospheric boundary layer. *Bound.-Lay. Meteorol.* **1999**, 91, 145–157.

[59] STOLL, J.; PORTÈ-AGEL, F. Dynamic subgrid-scale models for momentum and scalar fluxes in large-eddy simulations of neutrally stratified atmospheric boundary layers over heterogeneous terrain. *W. Resour. Research* **2006**, 42, W01409.

[60] Stoll, J.; Portè-Agel, F. Large-Eddy Simulation of the Stable Atmospheric Boundary Layer using Dynamic Models with Different Averaging Schemes. *Bound.-Lay. Meteorol.* **2008**, 126, 1–28.

[61] Stull, R. B. *An introduction to boundary layer meteorology*; Kluwer Academic Publishers: The Netherlands, 1988.

[62] Thomson, D. J. Criteria for teh selection of stochastic models for particle trajectories in turbulent flows. *J. Fluid Mech.* **1987**, 180, 529–556.

[63] Taylor, G. I. Diffusion by continuous movements. *Proc. Lond. Math Soc.* **1921**, 20, 196–212.

[64] Uliasz, M. Lagrangian particle dispersion modeling in mesoscale applications. *Env. Modeling - Vol. II.* **1994**, 71–101.

[65] Voller, V. R; Portè-Agel, F. Moore's law and numerical modeling. *J. Comp. Phys.* **2002**, 179, 698–703.

[66] Wang, H.; Takle, E. S. Boundary-Layer flow and turbulence near porous obstacles: I. Derivation of a general equation set for a porous medium. *Bound.-Lay. Meteorol.* **1995**, 74, 73–88.

[67] Weil, J. C.; Sullivan, P. P.; Moeng, C. The use of large-eddy simulations in lagrangian particle dispersion models. *J. Atmos. Sci.* **2004**, 61, 2877–2887.

[68] Wesely, M. L.; Hicks, B. B. A review of the current status of knowledge on dry deposition. *Atmos. Env.* **2000**, 34, 2261–2282.

[69] Wilcox, D. C. *Turbulence Modeling for CFD;* DCW Industries Inc.: La Cañada, 2006.

[70] Willis, G. E.; Deardorff, J. W. A laboratory model of diffusion into the convective planetary boundary layer. *Quart. J. Roy. Meteorol. Soc.* **1976**, 102, 427–445.

[71] Wilson, N. R.; Shaw, R. H. A higher order closure model for canopy flow. *J. Applied Meteorol.* **1977**, 16, 1197–1205/

[72] Wilson, N. R.; Thurtell, G. W.; Kidd, G. E. Numerical simulation of particle trajectories in inhomogeneous turbulence, I: Systems with constant turbulent velociy scale. *Bound.-Lay. Meteorol.* **1981a**, 21, 295–313

[73] Wilson, N. R.; Thurtell, G. W.; Kidd, G. E. Numerical simulation of particle trajectories in inhomogeneous turbulence, II: Systems with variable turbulent velocity scale. *Bound.-Lay. Meteorol.* **1981b**, 21, 423–441

[74] Wilson, N. R.; Thurtell, G. W.; Kidd, G. E. *Numerical simulation of particle trajectories in inhomogeneous turbulence, III: Comparisons of predicitions with experimental data for the atmospheric surface layer. Bound.-Lay. Meteorol.* **1981c**, 21, 163–169

[75] WONG, J. B.; RANZ, W. E.; JOHNSTONE, H. F. Inertial impaction of aerosol particles on cylinders. *J. Appl. Phys.* **2009**, 26, 244–249.

[76] WYNGAARD, J. C.; COTÉ, O., R. The evolution of the convective planetary boundary layer-A higher-order closure model study. *Bound.-Lay. Meteorol.* **1974**, 7, 289–308.

[77] YAMADA, T.; MELLOR, G. A simulation of the Wangara atmospheric boundary layer data. *J. Atmos. Sci.* **1975**, 32, 2309–2329.

[78] YEE, E.; WILSON, J. D. Instability in Lagrangian stochastic trajectory models and a method for its cure. *Bound.-Lay. Meteorol.* **2007**, 122, 243–261.

[79] YUE, W.; PARLANGE, M. B.; MENEVEAU, C.; ZHU, W.; VAN HOUT, R.; KATZ, J. Large-eddy simulation of plant canopy flows using plant-scale representation. *Bound.-Lay. Meteorol.* **2007**, 124, 183–203.

[80] ZEMAN, O.; LUMLEY, J. L. Modeling buoyancy driven mixed layers. *J. Atmos. Sci.* **1976**, 33, 1974–1988.